1 **Assimilation of blended in situ-satellite snow water equivalent into the National Water**

2 **Model for improving hydrologic simulation in two US river basins**

3

4 Yanjun Gan[1,*], Yu Zhang[1,*], Yuqiong Liu[2], Cezar Kongoli[3], Christopher Grassotti[3]

5 [1]Department of Civil Engineering, University of Texas at Arlington, Arlington, TX, USA

6 [2]LEN Technologies, Inc, Oak Hill, VA, USA

7 [3]Earth System Science Interdisciplinary Center, University of Maryland, College Park, College

8 Park, MD, USA

9

12

13 * Corresponding authors. E-mail addresses: yanjun.gan@uta.edu (Y. Gan), yu.zhang@uta.edu

14 (Y. Zhang).

Abstract

15

16   This study investigates the potential of assimilating a 1/8° blended in situ-satellite snow water

17   equivalent (SWE) product for improving snow and streamflow predictions of the National Water

18   Model (NWM). The blended product is assimilated into the NWM via a three-dimensional

19   variational (3DVAR) scheme and a direct insertion (DI) scheme, with a daily (1d) and a every 5

20   days (5d) assimilation frequencies. The experiments are for the Upper Colorado River Basin

21   (UCRB) and Susquehanna River Basin (SRB), which feature seasonal and ephemeral snow covers,

22   respectively. Results indicate that 3DVAR with a 5d assimilation frequency generally outperforms

23   the other scenarios. The assimilation of the blended SWE product mitigates the underestimation

24   of SWE evident in the open-loop simulations for both basins and its impacts are more pronounced

25   for UCRB than for SRB since snowfall is the main source of precipitation in the former.

26   Assimilation leads to improved streamflow over a majority of SRB subbasins, but over a minority

27   of UCRB subbasins. The degradations in streamflow for UCRB subbasins are mainly caused by

28   the overestimated SWE. In addition, the open-loop simulation often produces an earlier streamflow

29   peak in UCRB, and this error is mitigated to a limited extent by assimilation. These findings in

30   aggregate suggest that the efficacy of snow assimilation is strongly dependent upon the types of

31   snowpack and differential assimilation methods and frequencies.

32   **Keywords**: National Water Model; snow data assimilation; snow water equivalent; streamflow

33   prediction; passive microwave; 3DVAR.

34   **Abbreviations**: SWE, snow water equivalent; SD, snow depth; ST, snow temperature; OL, open-

35   loop; DA, Data assimilation; 3DVAR, three-dimensional variational; 3DVAR1, 3DVAR with a

36   daily assimilation frequency; 3DVAR5, 3DVAR with a every 5 days assimilation frequency; DI,

37   direct insertion; DI1, DI with a daily assimilation frequency; DI5, DI with a every 5 days

38   assimilation frequency; UCRB, Upper Colorado River Basin; SRB, Susquehanna River Basin;

39   NWM, National Water Model; NWM V2.0, NWM version 2.0; WRF, Weather Research and

40   Forecasting; WRF-Hydro, WRF hydrological modeling system; Noah-MP, Noah-

41   multiparameterization model; RTM, radiative transfer model; PMW, passive microwave; AMSR-

42   E, Advanced Microwave Scanning Radiometer for Earth Observing System; SMMR, Scanning

43   Multichannel Microwave Radiometer; ATMS, Advanced Technology Microwave Sounder;

44   AMSR2, Advanced Microwave Scanning Radiometer 2; SNOTEL, snow telemetry; COOP,

45   Cooperative Observer Network; CONUS, conterminous US; USGS, U.S. Geological Survey;

46   NOHRSC, National Operational Hydrologic Remote Sensing Center; NLDAS-2, North American

47   Land Data Assimilation System project phase 2; SNODAS, Snow Data Assimilation System; RB,

48   relative bias; RMSE, root-mean-square error; CC, Pearson correlation coefficient.

1. Introduction

Accurate, timely estimation and forecast of snowpack are of critical importance for water resources management and flood preparedness over regions with sizable snow cover (Dozier et al., 2016; Lievens et al., 2019; Pulliainen et al., 2020). At present, hydrologic predictions over such regions often involve simulation of snowpack and its evolution using snow models, which represent processes including snow accumulation, metamorphosis, blowing snow, and snow ablation (Essery et al., 2013; Magnusson et al., 2015). Snowmelt is then fed to water balance and routing models to compute streamflow. In many cases, errors in the model representation of snowpack have been a major source of uncertainties in the streamflow prediction (Franz et al., 2010). These errors stem from uncertainties associated with model structures (Gan et al., 2019; Zhang et al., 2016), parameters (Arsenault et al., 2018; Gan et al., 2018), initial conditions and forcing data (Raleigh et al., 2015; Terzago et al., 2020).

To account for and reduce such errors, various mechanisms for assimilating snowpack observations have been introduced (Helmert et al., 2018; Liu et al., 2012). In the US, forecasters in the National Weather Service (NWS) River Forecast Centers (RFCs) regularly employ in situ observations to adjust the snowpack states in their Snow-17 model (Anderson, 1973; Franz et al., 2008). A number of authors have also explored the assimilation of in situ snow observations (Huang et al., 2017; Liston and Hiemstra, 2008; Magnusson et al., 2014; Smyth et al., 2020), and the outcomes in general suggest that snow assimilation has very limited improvements in large-scale simulations due to the small spatial coverage of the in situ data (Liu et al., 2013; Thirel et al., 2013).

Over the past few decades, a number of space and air-borne snow observational platforms have come online, offering a variety of remotely sensed snow products that could be integrated

72 into snow and hydrologic models (Dietz et al., 2012; Frei et al., 2012). Data assimilation (DA) of

73 remotely sensed snow retrievals has focused on satellite-based snow cover (Clark et al., 2006;

74 Teweldebrhan et al., 2019; Thirel et al., 2013; Toure et al., 2018; Zhang et al., 2014) and snow

75 albedo (Kumar et al., 2020; Malik et al., 2012; Molotch et al., 2004; Wang et al., 2015), because

76 they are more direct observations from the visible or near-infrared sensors and have relatively

77 higher resolutions and smaller observation errors than the snow mass sensed by passive microwave

78 (PMW) sensors (Dong, 2018; Dozier et al., 2016). These experiments generally led to visible

79 improvements in snowpack simulations for basins with ephemeral snow, which means snowpack

80 that persists for < 60 continuous days and melts and sublimates throughout the snow cover season

81 instead of having one consistent period of snowmelt (Petersky and Harpold, 2018; Sturm et al.,

82 1995). However, limited, if any, improvements were reported for basins with seasonal snow,

83 because snow cover/albedo data provide little information beyond the first and last few weeks of

84 the long snow season (Clark et al., 2006; Zaitchik and Rodell, 2009).

85   Results from previous attempts of assimilating remotely sensed PMW snow depth (SD) or

86 snow water equivalent (SWE) were not encouraging, due to large errors as well as limited spatial

87 representativeness of PMW SD/SWE retrievals (Dozier et al., 2016; Liu et al., 2013). For example,

88 Andreadis and Lettenmaier (2006) assimilated the Advanced Microwave Scanning Radiometer for

89 Earth Observing System (AMSR-E)-derived SWE observations into the Variable Infiltration

90 Capacity (VIC) model but reported a degradation of model estimates due to the large errors in the

91 AMSR-E SWE product. Dong et al. (2007) assimilated the Scanning Multichannel Microwave

92 Radiometer (SMMR)-derived SWE observations into a catchment-based land surface model and

93 demonstrated that assimilation algorithm was no longer able to improve SWE simulation when the

94 simulated SWE is beyond the 100 mm cutoff. Some researchers suggested assimilating radiometric

95 quantities directly, applying a radiative transfer model (RTM) to relate radiometric measurements

96 to SD/SWE within the assimilation scheme (Durand and Margulis, 2007; Kwon et al., 2017; Li et

97 al., 2017). Nonetheless, RTM errors may propagate through the DA system and ultimately degrade

98 snow estimates (Andreadis et al., 2008; Durand et al., 2008).

99 There have been attempts to preprocess PMW SD/SWE estimates to facilitate their

100 assimilation into snow and land surface models. These include De Lannoy et al. (2012), wherein

101 an anomaly-based scaling approach was conceived to adjust the time-smoothed AMSR-E SWE

102 products, and Liu et al. (2015), in which a blended SD product was created that combines AMSR-

103 E SD retrieval with in situ observations. While the latter study demonstrated considerable overall

104 improvement in the prediction of snowpack after assimilation, the earlier one failed to improve

105 SWE after assimilation of the scaled product, because although the magnitude of the SWE peak

106 climatology can be effectively adjusted, the timing of onset and melt was not correctly scaled and

107 the interannual variations cannot be corrected.

108 The objective of this paper is to investigate the potential of assimilating a recently developed

109 in situ-satellite blended SWE product for improving snow and streamflow simulations of the

110 National Water Model (NWM). This product, developed by Gan et al. (2021), blends two PWM

111 SWE products that undergo bias adjustment using in situ observations. These products are the

112 SWE retrievals from Suomi National Polar-orbiting Partnership (S-NPP) Advanced Technology

113 Microwave Sounder (ATMS; Weng et al., 2012) and Global Change Observation Mission – Water

114 (GCOM-W1) Advanced Microwave Scanning Radiometer 2 (AMSR2; Kelly, 2009). This blended

115 SWE product is assimilated into the operational NWM through a newly developed snow

116 assimilation strategy. Chosen as the study areas are the Upper Colorado River Basin (UCRB) and

117 Susquehanna River Basin (SRB) in the US, featuring seasonal and ephemeral snow covers,

118 respectively. While this investigation in some ways mirrors Liu et al. (2015), it features a different

119 set of science questions: 1) how impacts of SWE assimilation differ for snowpack and streamflow

120 over basins dominated by seasonal and ephemeral snowpack? 2) what are the specific merits of

121 DA algorithms such as direct insertion (DI) and three-dimensional variational assimilation

122 (3DVAR) in alleviating probable biases in snowpack and streamflow? and 3) how SWE

123 assimilation differentially impacts various components of hydrologic cycle as represented by the

124 model? By addressing these questions, the study offers insights into the potential constraints to the

125 efficacy of SWE assimilation that are rooted in model structure and parameterization.

126 The remainder of this paper is organized as follows. Section 2 describes the study areas and

127 data. Section 3 introduces the model, methods, and experimental setup. Results are described and

128 discussed in Section 4. Section 5 summarizes the findings and offers concluding remarks.

129 **2. Study areas and data**

130 **2.1. Study areas**

131 The UCRB and SRB were chosen as our study areas, in which the snow cover is seasonal for

132 the former and ephemeral for the latter. We selected 67 UCRB subbasins and 54 SRB subbasins

133 that have continuous streamflow records and SD/SWE records for at least one snow survey site

134 during the water years 2017–2019. Figure 1 shows the spatial distributions of elevation, snow

135 telemetry (SNOTEL) and Cooperative Observer Network (COOP) snow survey sites, US

136 Geological Survey (USGS) streamflow gauging stations, and subbasins in the two river basins.

137 Detailed information of all the selected USGS stations is given in Table S1. The COOP and

138 SNOTEL sites information can be found at https://mesonet.agron.iastate.edu/COOP and

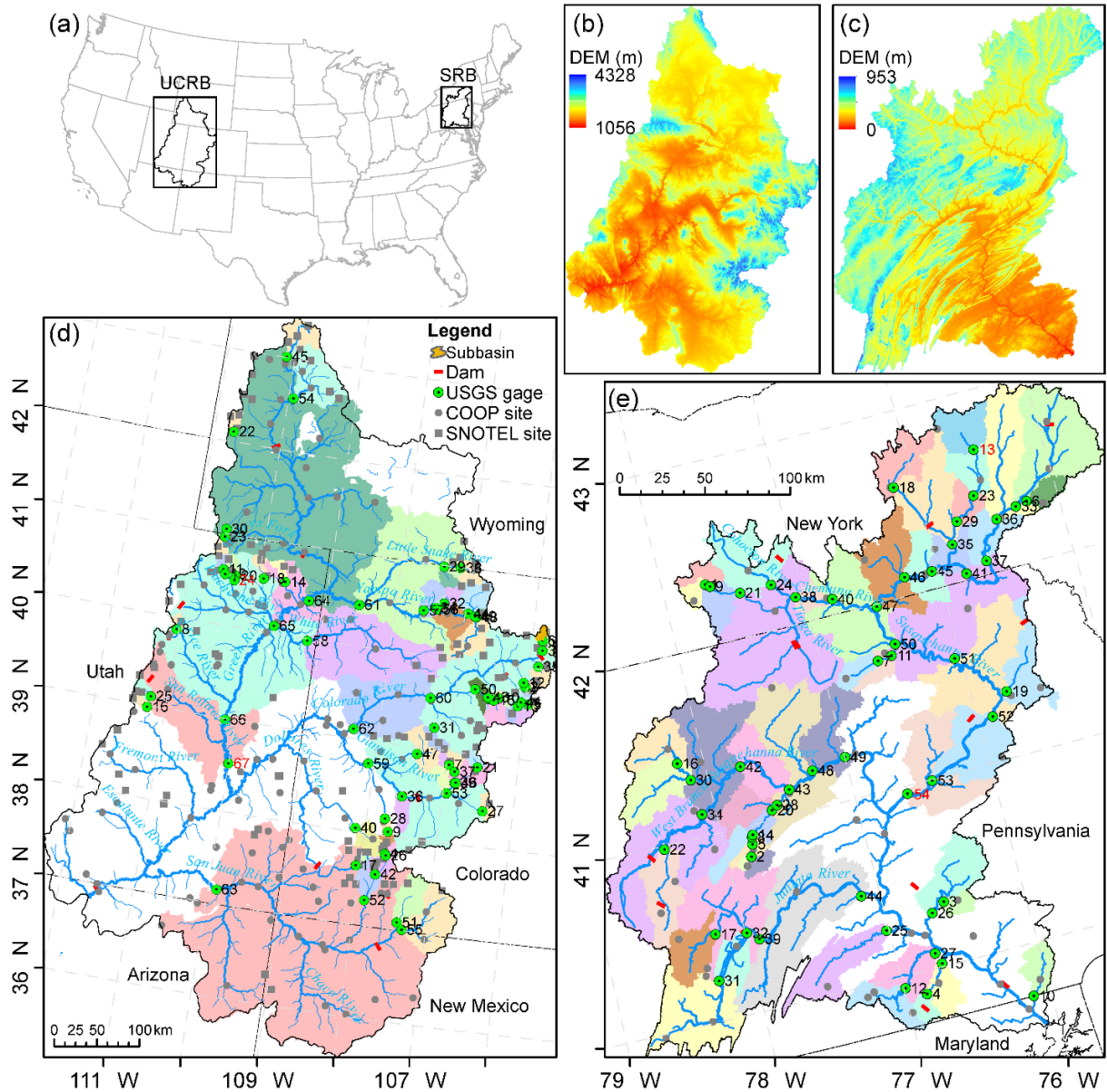139 https://www.wcc.nrcs.usda.gov/snow, respectively.

Figure 1. (a) locations of the UCRB and SRB in the US, (b) UCRB elevation, (c) SRB elevation, (d) UCRB selected subbasins and observation stations, and (e) SRB selected subbasins and observation stations. Note that some larger subbasins may consist of a few smaller subbasins. The number besides each station shows its ID, which is the rank in ascending order of drainage area. For each basin, a pair of subbasins were chosen for demonstration, with their IDs are denoted in red color. Detailed information of the gauging stations, including the name, latitude, longitude, feature ID, drainage area, etc., can be found in Table S1.

The Upper Colorado River starts in the central Rocky Mountains of Colorado, flows southwest across the Colorado Plateau, and reaches the Lee's Ferry in northern Arizona. The

151 UCRB covers a geographical area from 35.5°N to 43.5°N and 105.5°W to 112.5°W with a drainage

152 area of about 277,000 km^2. The physiography is rather heterogeneous for UCRB, which has an

153 elevation range of 1056–4328 m with an average elevation of 2146 m. Land cover in UCRB

154 includes 57% shrubland, 22% evergreen needleleaf, 7% deciduous broadleaf forest, 7% grassland,

155 and 4% barren or sparsely vegetated as determined from the USGS land cover data. Snow accounts

156 for about 63% of the annual precipitation in the UCRB, and mainly falls and remains frozen during

157 the winter months (November–April) until the warm season when snowpack begins to melt

158 (starting in late April or early May) (Liu et al., 2015).

159   The 715-km long Susquehanna River is the longest river on the East Coast of the US with an

160 outlet to the Chesapeake Bay. The SRB covers a geographical area from 39.5°N to 43°N and

161 74.5°W to 79°W with a drainage area of about 71,228 km^2. It has an elevation range of 0–953 m

162 with an average elevation of 391 m. The SRB is covered by 61% deciduous broadleaf forest, 16%

163 dryland cropland and pasture, 11% irrigated cropland and pasture, 6% mixed forest, and 3% urban

164 and built land as determined from the USGS land cover data. Most of the winter precipitation

165 within the SRB is in the form of snowfall, which mostly occurs in the northern part of the basin

166 during the period of December–March (Suriano et al., 2020).

167   Among all selected subbasins, we chose a pair of them (a small one and a large one) for both

168 UCRB (IDs 24 and 67; stations 09292500 and 09328920) and SRB (IDs 13 and 54; stations

169 01505000 and 01540500) to demonstrate the time series of spatial-averaged daily SWE and outlet

170 streamflow in Section 4.3.4. The two chosen UCRB subbasins drain into the Green River, which

171 is the longest headwater tributary of the Colorado River and is dominated by spring snowmelt. The

172 two chosen SRB subbasins are located in the northern SRB, where most snow events occur.

173 **2.2. Data**

174   We used the static and forcing data to run the model, the observation data to assimilate into

175   the model, and the reference data to validate the model. A summary of all the datasets is provided

176   in Table 1. A detailed description of them is given below.

177   **Table 1.** Experimental data used in this study.

Data category	Data name	Spatial resolution	Temporal resolution	Reference/Availability
Static data	Land-related data	1 km	N/A	https://water.noaa.gov/about/nwm
	Routing-related data	250 m	N/A	https://water.noaa.gov/about/nwm
Forcing data	NLDAS-2 forcing	1/8°	hourly	Xia et al. (2012a); https://doi.org/10.5067/6J5LHHOHZHN4
Observation data	Blended in situ-satellite SWE data	1/8°	daily	Gan et al. (2021); https://www.hydroshare.org/resource/7ac869e3be06411d8f43bf152b62a755
Reference data	SNODAS SWE	1 km	daily	Carroll et al. (2001); https://nsidc.org/data/G02158
	USGS streamflow	gauge	daily	https://waterdata.usgs.gov/nwis/dv/?referred_module=sw

178

179 **2.2.1. Static data**

180   The static data for the two research domains were acquired by subsetting the conterminous

181   US (CONUS) statistic data downloaded from the National Water Center (NWC). The 1 km × 1

182   km land surface model grid and relevant geospatial data such as land cover and soil properties

183   were processed from the geographical static data using Weather Research and Forecasting (WRF)

184   model Preprocessing System (WPS; Wang et al., 2017). The 250 m × 250 m routing-related static

185   data such as the elevation, flow direction, and stream order were processed from the National

186   Hydrography Dataset Plus Version 2 (NHDPlusV2; McKay et al., 2012) using WRF-Hydro GIS

187   Pre-processor v5 (Sampson and Gochis, 2020).

2.2.2. Forcing data

We used the WRF-Hydro meteorological forcing engine (Zhang et al., 2020) to prepare input data from the North American Land Data Assimilation System project phase 2 (NLDAS-2; Xia et al., 2012a). The 1/8° hourly NLDAS-2 forcing dataset for the water years 2016–2019 was first remapped to the 1-km research domains by bilinear interpolation. Various downscaling methods were then used to adjust the forcing variables to account for the differences in topographic characteristics (e.g., elevation, slope, and aspect) between the 1-km NWM grid cells and 1/8° NLDAS-2 grid cells. The forcing variables including 2-m air temperature (K), 2-m specific humidity (kg kg^{-1}), surface pressure (Pa), and downward shortwave radiation (W m^{-2}) were adjusted using the methods in WRF-Hydro meteorological forcing engine (Zhang et al., 2020). Precipitation rate (mm s^{-1}) was adjusted using the method in Liston and Elder (2006). Downward longwave radiation (W m^{-2}) and 10-m wind speed at u and v directions (m s^{-1}) were not adjusted. Multi-year (water years 2016–2019) mean data of the forcing variables for the two river basins are given in Figure S1.

2.2.3. Observation data

A 1/8° daily blended in situ-satellite SWE dataset was produced to provide gridded observations for DA (Gan et al., 2021). This dataset is based on PMW SWE retrievals from the ATMS and AMSR2 as well as daily in situ SD/SWE observations from the COOP/SNOTEL networks. COOP daily SD data were converted to SWE using the snow bulk density method (Sturm et al., 2010) considering the effects of SD, snow aging, and snow cover classes. Level 2 ATMS and AMSR2 data at the raw satellite observation field of views were binned into gridded fields of daily SWE on a resolution of 1/8° latitude/longitude as in NLDAS-2 grid cells. The blended product was then generated by 1) snow cover mask of the PMW SWE retrievals using the

211 Interactive Multisensor Snow and Ice Mapping System (IMS) snow cover maps, 2) Cumulative

212 distribution function (CDF) matching-based bias correction of the masked PMW SWE retrievals

213 using in situ observations, 3) optimal interpolation of the bias corrected PMW SWE retrievals with

214 in situ observations, and 4) weighted averaging of the ATMS- and AMSR2-based SWE products.

215 Detailed algorithm can be found in Gan et al. (2021). This dataset was shown to have good

216 reliability through cross-validation against SNOTEL/COOP sites observations (Gan et al., 2021).

217 It should be noted that the blended product subjects to uncertainties stemming from the PMW

218 SWE retrievals caused by factors such as instrument error, sensor saturation, and retrieval

219 algorithm. The uncertainties of the blended product, therefore, are location dependent, and likely

220 smaller in grid cells where there are ground observations (i.e., SNOTEL and COOP sites) and

221 possibly larger where there are not. Maps showing the multi-year mean daily SWE in different

222 months over the CONUS can be found in Figure 12 of Gan et al. (2021).

223 **2.2.4. Reference data**

224 There are no high-resolution SWE observations across large domain. The National

225 Operational Hydrologic Remote Sensing Center (NOHRSC) Snow Data Assimilation System

226 (SNODAS) provides a 1-km daily SWE product over the CONUS (Carroll et al., 2001). Although

227 it is not an observational product, SNODAS takes the physically based energy- and mass-balance

228 NOHRSC Snow Model (NSM) as the primary component and assimilates snow observations from

229 satellite, airborne platforms, and ground stations. Note that SNODAS shares some data sources

230 such as the SNOTEL SWE and COOP SD with the blended products and therefore does not

231 constitute a completely independent data source. Nonetheless, it is a mature and widely used

232 operational product that is of relatively reliable quality and high resolution (Barlage et al., 2010;

233 Gyawali and Watkins, 2013; Kumar et al., 2020; Liu et al., 2015; Wrzesien et al., 2017). In this

234 study SNODAS product serves as a benchmark that we will compare NWM SWE simulations

235 against, since it has the same resolution as NWM and also integrates model simulations with

236 observations as our NWM DA products. The primary aim of the comparison is to identify

237 discrepancies that may be potential indications of errors or biases. We downloaded SNODAS SWE

238 data from the National Snow and Ice Data Center (NSIDC) and resampled them into our model

239 grid using bilinear interpolation.

240   The daily streamflow discharge data for the 67 UCRB gauging stations and 54 SRB gauging

241 stations were acquired from the USGS.

242 **3. Methodology**

243 **3.1. National Water Model configuration**

244   The NWM version 2.0 (NWM V2.0) is adopted in this study for hydrologic simulation, with

245 the details of its snow physics are given in the Appendix A. The core of the NWM is the WRF-

246 Hydro (Gochis et al., 2018), which is a physically-based distributed land surface/hydrologic model

247 configured to use the Noah-multiparameterization model (Noah-MP; Niu et al., 2011) to simulate

248 land surface processes. Noah-MP provides a plethora of physical configurations and multiple

249 parameterization options. We adopted the default physical configurations (Table S2) and model

250 parameters (https://water.noaa.gov/about/nwm) of the operational NWM V2.0. Note that NWM

251 parameters had been calibrated for streamflow simulation in some river basins by National Center

252 for Atmospheric Research (NCAR) NWM team before its operational use. Detailed information

253 regarding the calibrated parameters and calibration strategy can be found in RafieeiNasab et al.

254 (2020) and the information whether the UCRB and SRB subbasins are calibrated or not is given

255 in Table S1.

256   The model spatial resolution was set to 1-km with an hourly timestep for the land surface

257   processes simulation. The subgrid overland routing was executed on a 250-m grid mesh and the

258   timesteps for terrain and channel routing were set to 10 and 300 seconds, respectively. Using the

259   National Centers for Environmental Prediction (NCEP) Final (FNL) Operational Global Analysis

260   data (National Centers for Environmental Prediction/National Weather Service/NOAA/U.S.

261   Department of Commerce, 2000) as the initial conditions, NWM was run by recycling the NLDAS-

262   2 forcing from 1 October 2015 to 30 September 2019 for five cycles (20 years). This long spin-up

263   run is to make the model to reach an equilibrium state for soil temperature and moisture as well as

264   groundwater. A series of experiments were then conducted for the water years 2016–2019, in

265   which the results of the first water year were excluded for analyses to further minimize the

266   influence of uncertainties in the initial conditions. Land surface outputs were generated at 0:00

267   every day and the hydrologic outputs were generated every 3 h from 0:00 to 21:00.

268   **3.2. Assimilation strategy**

269   DA experiments were performed similarly as the open-loop (OL) experiments using the same

270   settings except that they assimilated the blended SWE data daily or every 5 days during the period

271   of November 1–April 30 of the water years 2017–2019. Figure 2 shows a flowchart of the

272   assimilation procedure. NWM is run forward in time, up to a point when assimilation is activated.

273   At each assimilation step (0:00 UTC of the day), NWM would be stopped first and predicted SWE

274   at each grid cell is updated with the blended SWE of the same day using different DA methods.

275   SD is then adjusted based on the physical relationship of the updated SWE and model-predicted

276   snow density. Next, the updated SWE and SD are redistributed to different snow layers following

277   Noah-MP's three-layer snow model (Yang and Niu, 2003; see also the Appendix A). Snow

278   temperature of each layer is updated based on the following rules: 1) when snow is observed and

279 predicted by the model in that layer, snow temperature is same as the model predicted; 2) when

280 snow is observed but not predicted by the model in that layer, snow temperature is set to that of

281 the lower neighboring layer or the ground when there is no predicted snow. After updating the

282 snow properties, NWM is then restarted to run until the next assimilation step. At each assimilation

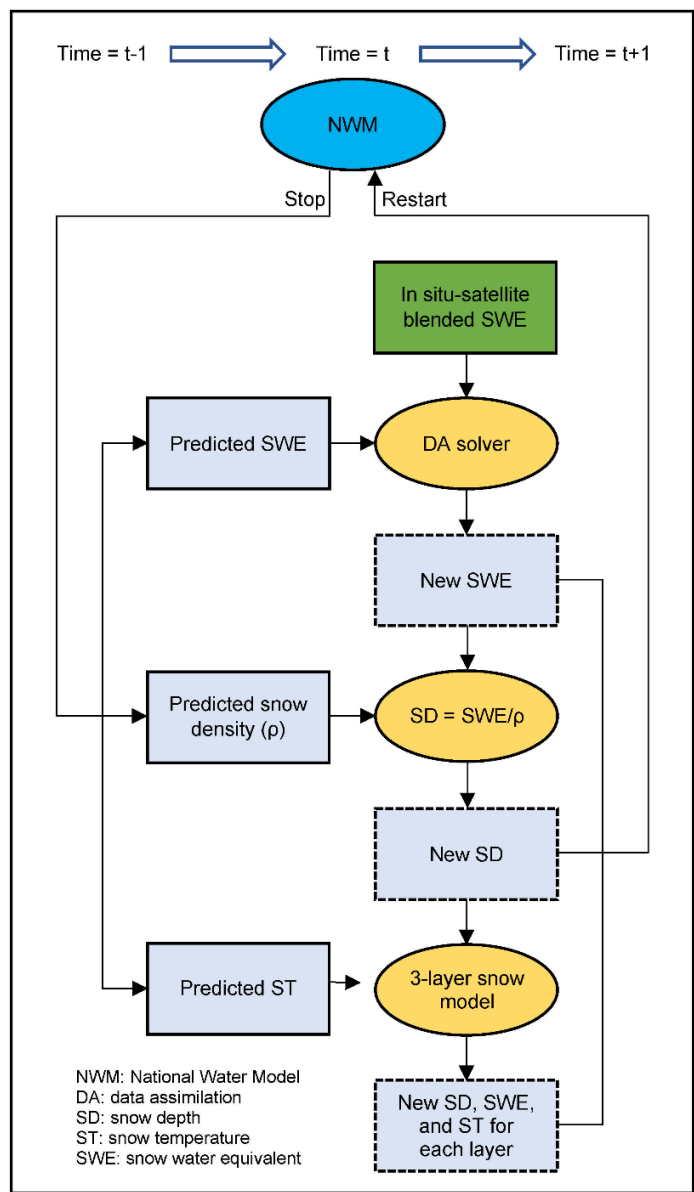283 step, the predicted SWE and streamflow prior to the assimilation are saved for subsequent

284 comparison.

285

286 **Figure 2.** Flowchart showing the assimilation procedure. At each assimilation step, the model will
287 be stopped first, then SWE, SD, and ST will be updated for each layer, and finally all the other
288 snow-related variables will be updated based on the updated SWE, SD, and ST by restarting the
289 model. The blue boxes represent model state variables, and the green box represents the
290 observations.
291

292 **3.3. Assimilation methods**

293 There are several methods that have been used for snow DA, ranging from simple approaches

294 such as DI (Talagrand and Miyakoda, 1971), to relatively sophisticated approaches such as optimal

295 interpolation (OI; Gandin, 1965) and variational (VAR; Sasaki, 1958), to more sophisticated

296 approaches such as Kalman filter (KF; Kalman, 1960), extended Kalman filter (EKF; Gelb, 1974),

297 ensemble Kalman filter (EnKF; Evensen, 1994), and particle filter (PF; Del Moral, 1996). A review

298 of the snow DA methods, including their merits and drawbacks was given by Helmert et al. (2018).

299 The DA methods we adopted include the 3DVAR and DI, which are relatively easy to implement

300 and computationally efficient.

3.3.1. Three-dimensional variational assimilation

302 The goal of 3DVAR is to produce an optimal estimate of the true state $\mathbf{x}$ at analysis time

303 through an iterative solution that minimizes a prescribed cost function

$$J(\mathbf{x}) = \frac{1}{2}(\mathbf{x} - \mathbf{x}_b)^{\mathrm{T}}\mathbf{B}^{-1}(\mathbf{x} - \mathbf{x}_b) + \frac{1}{2}\big(\mathbf{y}_o - H(\mathbf{x})\big)^{\mathrm{T}}\mathbf{R}^{-1}\big(\mathbf{y}_o - H(\mathbf{x})\big) \tag{1}$$

305 where $\mathbf{x}_b$ is the background state; $\mathbf{B}$ is the background error covariance matrix; $\mathbf{y}_o$ is the

306 observation vector; H is the nonlinear observation operator used to transform the gridded analysis

307 $\mathbf{x}$ to observation space for comparison against observations; $\mathbf{R}$ is the observation error covariance

308 matrix; and the superscripts "T" and "−1" denote the transpose and inverse of the matrix,

309 respectively. The first and second terms on the right-hand side represent the background error

310 $J_b(\mathbf{x})$ and observation error $J_o(\mathbf{x})$, respectively. Quasi-Newton method is used to find the minimal

311 of the cost function.

312   By using the incremental method (Courtier et al., 1994), the solution of the minimization of

313    $J(\mathbf{x})$ is given by

314    $$\mathbf{x} = \mathbf{x}_b + \mathbf{K}\mathbf{d} \tag{2}$$

315   with the optimal gain matrix

316    $$\mathbf{K} = \mathbf{B}\mathbf{H}^{\mathrm{T}}(\mathbf{H}\mathbf{B}\mathbf{H}^{\mathrm{T}} + \mathbf{R})^{-1} \tag{3}$$

317   and the innovation vector

318    $$\mathbf{d} = \mathbf{y}_o - H(\mathbf{x}_b) = \big(\mathbf{y}_o - H(\mathbf{x}_t)\big) - \big(H(\mathbf{x}_b) - H(\mathbf{x}_t)\big) \approx \boldsymbol{\epsilon}_o - \mathbf{H}\boldsymbol{\epsilon}_b \tag{4}$$

319   where $\mathbf{H}$ is the observation operator linearized with respect to $\mathbf{x}_b$; $\mathbf{H}\mathbf{B}\mathbf{H}^{\mathrm{T}}$ can be interpreted as the

320   square matrix of the covariances of background errors in observation space while $\mathbf{B}\mathbf{H}^{\mathrm{T}}$ is the

321   rectangular matrix of the covariances between the background errors in model space and the

322   background errors in observation space; $\mathbf{x}_t$ is the unknown true state; $\boldsymbol{\epsilon}_o = \mathbf{y}_o - H(\mathbf{x}_t)$ is the

323   vector of observation errors; and $\boldsymbol{\epsilon}_b = \mathbf{x}_b - \mathbf{x}_t$ is the vector of background errors. Full details of

324   the procedure of the incremental variational assimilation algorithm could be found in Stewart et

325   al. (2013).

326   Following Hollingsworth and Lönnberg (1986), the error covariance matrices are diagnosed

327   from the observation-minus-background quantities (i.e., innovations), which are a combination of

328   background and observation errors as shown in the above equation. Assume that i and j are two

329   observation points (i.e., any two grid cells of the 1/8° blended SWE product), their innovation

330   covariance can be calculated as (Bouttier and Courtier, 2002)

331    $$\mathrm{cov}(i,j) = \overline{\mathbf{d}_i\mathbf{d}_j^{\mathrm{T}}} = \overline{(\mathbf{y}_i - \mathbf{H}_i\mathbf{x}_b)(\mathbf{y}_j - \mathbf{H}_j\mathbf{x}_b)^{\mathrm{T}}} =$$

332    $$\overline{[(\mathbf{y}_i - \mathbf{H}_i\mathbf{x}_t) + (\mathbf{H}_i\mathbf{x}_t - \mathbf{H}_i\mathbf{x}_b)]\big[(\mathbf{y}_j - \mathbf{H}_j\mathbf{x}_t) + (\mathbf{H}_j\mathbf{x}_t - \mathbf{H}_j\mathbf{x}_b)\big]^{\mathrm{T}}} = \overline{(\mathbf{y}_i - \mathbf{H}_i\mathbf{x}_t)(\mathbf{y}_j - \mathbf{H}_j\mathbf{x}_t)^{\mathrm{T}}} +$$

333    $$\mathbf{H}_i\overline{(\mathbf{x}_t - \mathbf{x}_b)(\mathbf{x}_t - \mathbf{x}_b)^{\mathrm{T}}}\mathbf{H}_j^{\mathrm{T}} + \overline{(\mathbf{y}_i - \mathbf{H}_i\mathbf{x}_t)(\mathbf{x}_t - \mathbf{x}_b)^{\mathrm{T}}}\mathbf{H}_j^{\mathrm{T}} + \mathbf{H}_i\overline{(\mathbf{x}_t - \mathbf{x}_b)(\mathbf{y}_j - \mathbf{H}_j\mathbf{x}_t)^{\mathrm{T}}} \tag{5}$$

334 where the overbar denotes the expectation; $\mathbf{y}_i$ and $\mathbf{y}_j$ are the observations (i.e., blended SWE data)

335 for observation points i and j, respectively; $\mathbf{H}_i$ and $\mathbf{H}_j$ are the observation operators used to

336 transform the background $\mathbf{x}_b$ (i.e., forecast from the previous analysis) to the observation points i

337 and j, respectively. The first term after the last equal sign is the observation error covariance

338 between i and j (i.e., $\mathbf{R}_{i,j}$); the second term is the background error covariance between i and j

339 (i.e., $\mathbf{H}_i \mathbf{B} \mathbf{H}_j^{\mathrm{T}}$); and the last two terms equal to zero if we assume that observation error and

340 background error are uncorrelated. The above equation can then be written as

$$341 \qquad \mathrm{cov}(i,j) \;=\; \begin{cases} \sigma_{o,i}^2 + \sigma_{b,i}^2, & i = j \\ \mathbf{H}_i \mathbf{B} \mathbf{H}_j^{\mathrm{T}}, & i \neq j \text{ and observation errors are uncorrelated} \end{cases} \qquad (6)$$

342 where $\sigma_{o,i}^2$ and $\sigma_{b,i}^2$ are the observation and background error variances for observation point i,

343 respectively. If $i \neq j$ and i and j are very close to each other, $\lim_{i \to j} \mathrm{cov}(i,j) = \sigma_{b,i}^2$, thus we can

344 determine $\sigma_{b,i}^2$ by determining the intercept for zero separation of $\mathrm{cov}(i,j)$, then we get the

345 observation error variance $\sigma_{o,i}^2 = \mathrm{cov}(i,j) - \sigma_{b,i}^2$ and the background error correlation $\mathrm{cov}(i,j)/$

346 $\sigma_{b,i}^2$ if the background error variances are homogeneous.

347   A schematic representation of the Hollingsworth-Lönnberg method is depicted in Figure 3.

348 The zero-separation bin provides averaged information about the background and observation

349 errors (i.e., observation and background error variances) and the nonzero-separation bins give the

350 averaged information about the background error only (i.e., background error covariance). The

351 background error covariance is negligible for very large separations. Here, we set the bin interval

352 to 25 km and the search radius to 400 km. Other application examples about the diagnostic of error

353 covariance matrices could be found in Järvinen (2001), Stewart et al. (2014) and Waller et al.
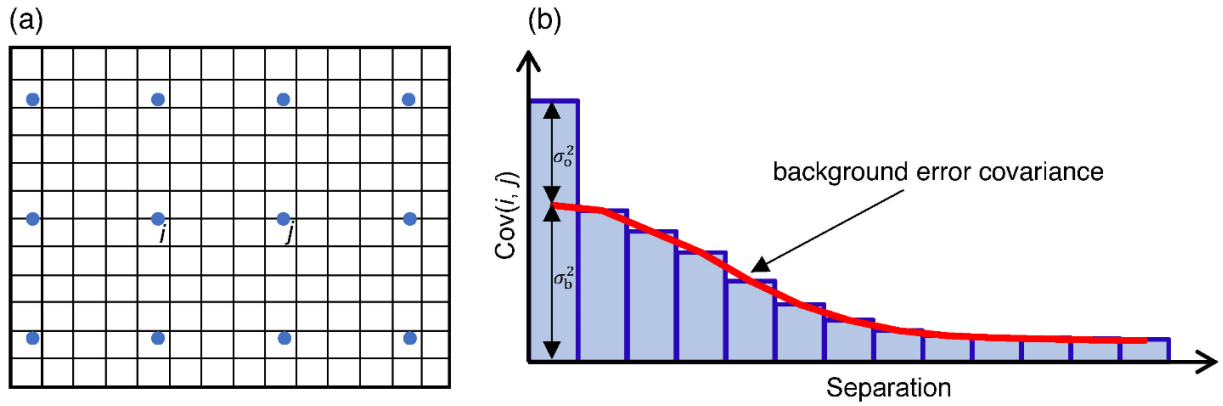
354 (2016).

Figure 3. Schematic representation of the Hollingsworth-Lönnberg method. Cov(i, j) is the innovation (observation − background) covariance between spatial points i and j. The innovation covariances are stratified against separation. The red line is an isotropic correlation model fit to the histogram and extrapolated to zero separation.

3.3.2. Direct insertion

As a benchmark test, we compared the assimilation results from 3DVAR with those from DI, which is often used in snow DA (Hedrick et al., 2018; Kumar et al., 2020). The major premises of DI are that observations are considered reliable and model simulations do not contain useful information. Model simulations can therefore be replaced by observations at each assimilation step. The 1/8° blended SWE product was remapped to our 1-km study areas by bilinear interpolation. We performed DI by directly substituting modeled SWE with the observations (i.e., 1-km blended SWE data) and indirectly adjusting SD as well as layer SWE, SD, and snow temperature using the above assimilation rules (Figure 2).

3.4. Experimental setup

Table 2 presents the layout of the experiments aimed at assessing the efficacy of assimilation methods and determining the optimal assimilation frequencies. An OL run was performed to create a baseline for the evaluation. Snow state variables were updated daily and every 5 days using the 3DVAR and DI methods to analyze their influences on SWE and streamflow. Model performances

375 were evaluated against different sources of reference data using relative bias (RB), root-mean-

376 square error (RMSE), and Pearson correlation coefficient (CC). RB measures the percentage of

377 bias of the modeled variable to the observed one, with a range between $-\infty$ and $+\infty$. A positive

378 /negative value of RB indicates overestimation/underestimation, and a smaller absolute value

379 indicates better model performance. RMSE measures the error magnitude between modeled and

380 observed variables, with a range between 0 and $+\infty$. A smaller value of RMSE indicates better

381 model performance. CC measures the closeness of the linear relationship between the modeled and

382 observed variables, with a range between -1 and 1. A positive/negative value of CC indicates a

383 positive/negative correlation, and a larger absolute value indicates stronger linear relationship.

384 **Table 2.** Experimental design for the comparison of assimilation methods and frequencies.

Case	Assimilation method	Assimilation frequency
OL	N/A	N/A
3DVAR1	3DVAR	Daily
3DVAR5	3DVAR	Every 5 days
DI1	DI	Daily
DI5	DI	Every 5 days

385 Note. OL = open loop; 3DVAR = three-dimensional variational assimilation; DI = direct insertion.
386 For the name of the case, the number after 3DVAR and DI indicates the assimilation frequency.
387
388 **4. Results and discussion**

389   In this section, we first evaluate modeled SWE and streamflow separately with different

390 reference datasets, and then we compare SWE and streamflow of the same subbasins to examine

391 their relationship.

392 **4.1. Evaluation of SWE**

393   Daily SWE simulations are compared against SNODAS SWE analysis. The relative accuracy

394 of SWE from different experiments (Table 2) are examined from the following perspectives: 1)

395 temporal variation of SWE and 2) spatial distribution of SWE.

4.1.1. Temporal variation of SWE

Figure 4 compares the spatial-averaged daily SWE from OL and DA experiments, as well as SNODAS analysis for UCRB and SRB. Although OL largely reproduces the seasonal evolution of SNODAS SWE, the magnitude of OL SWE is significantly lower than that of SNODAS, and this difference persists throughout the entire period in both basins (with a −29% RB in UCRB and a −34% RB in SRB). Note that SNODAS SWE is not necessarily the truth; nonetheless, this large difference may point to potential underestimation of SWE by the NWM. The low bias of modeled SWE can be mainly explained by the largely underestimated NLDAS-2 precipitation, which shows a 100–500 mm per year deficit over the high-elevation areas of the Western US (Henn et al., 2018). The other cause may be attributed to the low snow albedo as Noah-MP modeled (Chen et al., 2014; Kumar et al., 2020), which inflates absorbed radiation, increases available energy, and hence reduces snowpack. In addition, OL tracks the SNODAS phase more closely in UCRB than in SRB, although it also produces larger negative bias (15.0 mm RMSE for UCRB vs. 3.6 mm RMSE for SRB). This is reasonable because ephemeral snowpack prevailing in SRB is more difficult to be captured by model due to the more frequent and shorter accumulation-ablation processes in the same season (Petersky and Harpold, 2018).

The assimilation of the blended SWE product narrows the gap between NWM SWE and SNODAS analysis throughout the snow seasons evident in both basins. 3DVAR and DI generate spatial-averaged daily SWE time series that are comparable to those of SNODAS, which also assimilated SNOTEL SWE and COOP SD observations. Specifically, 3DVAR and DI with a daily assimilation frequency (3DVAR1 and DI1) reduce the RMSE in UCRB from 15.0 to 11.6 and 9.6 mm, respectively (Figure 4a); and applying the two mechanisms with a every 5 days assimilation frequency (3DVAR5 and DI5) reduce the RMSE from 15.0 to 8.4 and 10.3 mm, respectively

419   (Figure 4b). Meanwhile, they increase the RMSE in SRB from 3.6 to 6.3 and 6.5 mm, respectively,

420   regardless of the assimilation frequency (Figure 4c and d). It is noted that 3DVAR and DI show

421   similar performance even with different assimilation frequencies in SRB (Figure 4c and d),

422   whereas the former produces larger SWE than the latter when with a higher assimilation frequency

423   in UCRB (Figure 4a). This could be explained by the differing assimilation mechanisms of the two

424   methods. DI directly replaces model simulations with the observations (i.e., blended SWE data),

425   and naturally it yields analysis that approaches observations when assimilation frequency increases.

426   By contrast, 3DVAR blends model simulations with observations, which sometimes yields analysis

427   that would be larger than the observations when gradually increasing observations are assimilated

428   into the model with a sufficiently high frequency (i.e., 3DVAR1 in UCRB), and this may cause the

429   overshooting. Using a reduced assimilation frequency allows the model physics to gradually

430   compensate for the addition of SWE by DA, thus leading to physically more realistic results. It is,

431   therefore, reasonable that a lower assimilation frequency for 3DVAR (3DVAR5) and a higher

432   assimilation frequency for DI (DI1) lead to better agreements of the modeled SWE time series

433   with the SNODAS analysis in UCRB. In addition, DA experiments generally overestimate peak

434   SWE in both study areas and in most water years as compared to the SNODAS. The increases in

435   the SWE after performing DA may be an indication of improvement in snowpack simulations—

436   the SNODAS data were found to underestimate SWE as compared to in situ measurements

437   (Anderson, 2011; Gan et al., 2021) and lidar surveys (Hedrick et al., 2015), due to the

438   underestimated snow density (Anderson, 2011; Hedrick et al., 2015) and snow depth (Clow et al.,
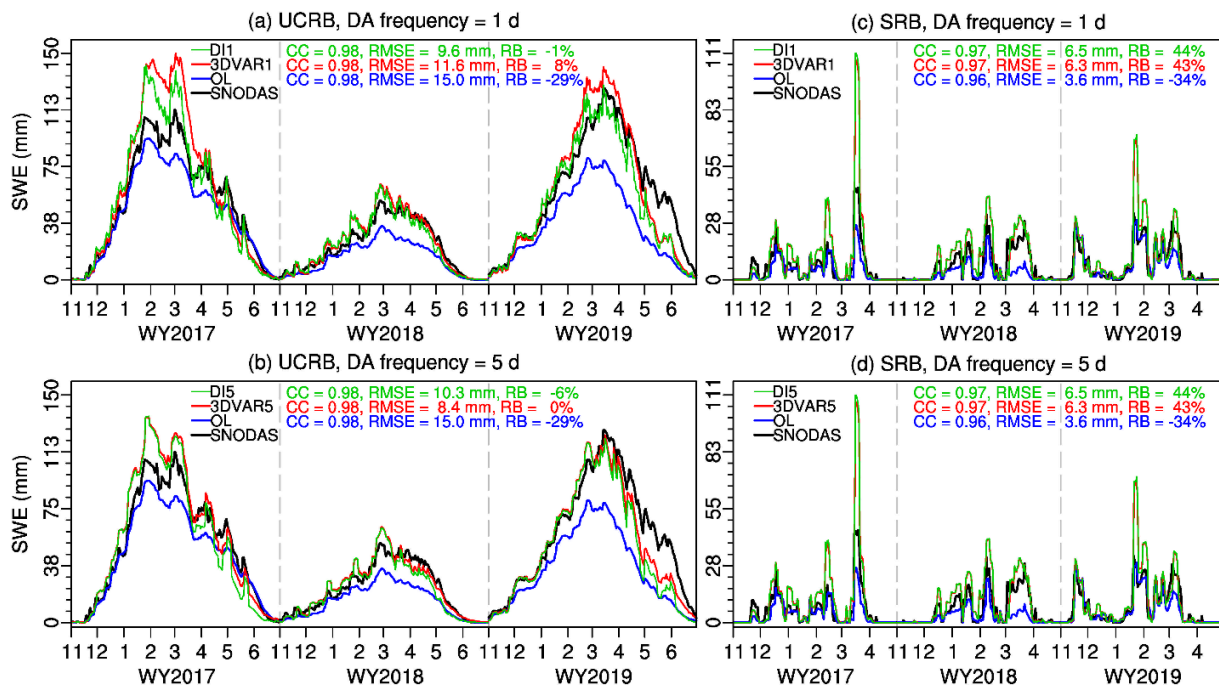
439   2012).

Figure 4. Time series of spatial-averaged daily SWE from different experiments during main snow seasons of the water years 2017–2019 for UCRB and SRB. DI, 3DVAR, OL, and SNODAS data are denoted by green, red, blue, and black lines with increasing thickness, respectively. CC, RMSE, and RB represent the correlation coefficient, root-mean-square error, and relative bias of model simulations against SNODAS analysis, respectively. Note that DA frequency is applicable only to DI and 3DVAR.

4.1.2. Spatial distribution of SWE

Figure 5 shows the spatial distributions of the muti-year mean daily SWE from the modeled (OL, 3DVAR1, DI1, 3DVAR5, and DI5), blended, and SNODAS for UCRB and SRB. Figure S2 presents the spatial distributions of the BIAS and CC of different SWE products against SNODAS analysis. OL produces lower SWE amounts in most snow regions of the UCRB and SRB relative to SNODAS analysis. It has a spatial-averaged bias of −10.6 and −0.8 mm for UCRB and SRB, respectively. 3DVAR and DI generally have similar spatial patterns, and all four DA experiments produce overall higher SWE values against SNODAS in most high-elevation zones of UCRB (Figure 5b–e) and in the northern and western mountainous zones of SRB (Figure 5i–l). However, the overestimation of the 3DVAR and DI may be reasonable since SNODAS analysis was reported

23

458 to underestimate SWE in these regions as stated before. On the other hand, the bias in low-

459 elevation zones (e.g., elevation $\leq$ 2000 m for UCRB and elevation $\leq$ 400 m for SRB; see Figure

460 1b and c for the spatial distribution of elevation) is less pronounced due to the much lower snow

461 accumulation in these zones; the differences among all five experiments are negligible (Figure 5a–

462 e for UCRB and Figure 5h–l for SRB). A higher assimilation frequency results in increased SWE

463 analysis (Figure 5b vs. d, c vs. e, i vs. k, and j vs. l) and the performance difference of assimilation

464 frequencies is more pronounced in UCRB than in SRB and for 3DVAR than for DI. 3DVAR with

465 a higher assimilation frequency (3DVAR1) generates highly heterogeneous SWE fields in UCRB

466 (Figure 5b) due to the cumulative effect of sequentially ingesting blended SWE product which

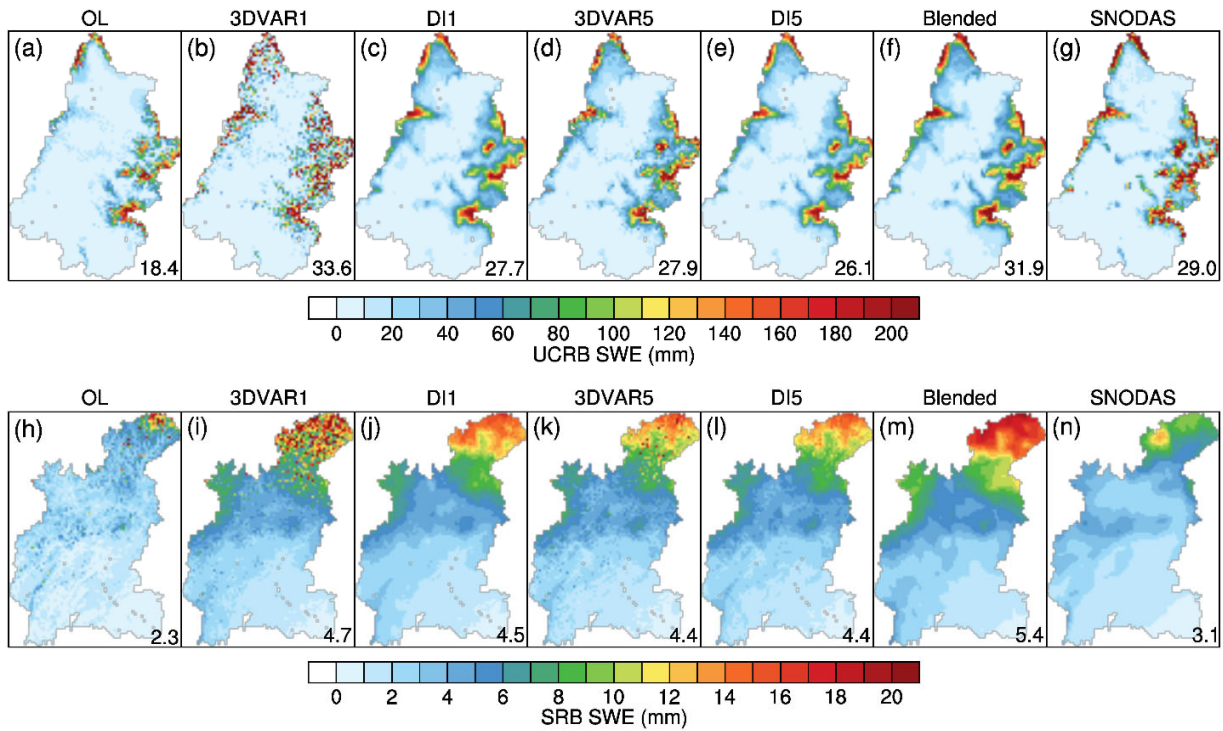467 exhibits relatively high spatial variability.

468
469 **Figure 5.** Spatial distributions of multi-year mean daily SWE from the OL, 3DVAR1, DI1,
470 3DVAR5, DI5, blended, and SNODAS during the water years 2017–2019 for UCRB and SRB.
471 The number on the bottom right corner of each subfigure presents the spatial-averaged value.
472

24

4.2. Evaluation of streamflow

Daily streamflow simulations are compared against USGS observations. Figure 6 presents the spatial distribution of RB and CC of modeled daily streamflow discharge for all selected gauges in the UCRB and SRB. OL has relatively good performance (i.e., small |RB| and high CC) in the eastern UCRB subbasins (upstream of the Colorado River) and in most of the SRB subbasins. Nevertheless, it underestimates streamflow for 85.1% of the UCRB subbasins (Figure 6a) and 83.3% of the SRB subbasins (Figure 6k). The underestimation of streamflow is mainly due to the underestimated precipitation and/or model deficiency in snow simulation, especially over the mountainous regions (Lohmann et al., 2004; Xia et al., 2012b). The assimilation of the blended SWE product mitigates the negative RB in streamflow and the effect is more pronounced for UCRB than for SRB due to the more severely underestimated streamflow in the OL experiment for the former (Figure 6a vs. k). Compared to the OL experiment, 3DVAR1, DI1, 3DVAR5, and DI5 reduce |RB| for 65.7%, 37.3%, 62.7%, and 64.2% of the UCRB subbasins, respectively, and for 74.1%, 70.4%, 75.9%, and 75.9% of the SRB subbasins, respectively. More SRB subbasins see improvements than do UCRB subbasins, although the degree of improvement is less pronounced in SRB. By contrast, UCRB subbasins have more severe overestimation of streamflow by DI1, which deteriorates |RB| for 62.7% of the subbasins (Figure 6c). This is because DI1 overestimates SWE for most upstream subbasins although it underestimates SWE overall for the entire UCRB. The overestimation of SWE by DI1 in the UCRB upstream subbasins could be attributed to the fact that the observations (i.e., blended SWE data) overestimate SWE in those subbasins and DI1 directly replaces model states with observations at every assimilation step. Considering both RB and CC, 3DVAR generally outperforms DI with the same assimilation frequency for streamflow simulation in most of the UCRB subbasins. 3DVAR/DI with a lower assimilation frequency

496 (3DVAR5/DI5) performs better than that with a higher assimilation frequency (3DVAR1/DI1) in

497 both basins because a higher assimilation frequency leads to more severe overestimation of SWE

498 and thus streamflow in more subbasins. It could also be noted that the performances of different

499 experiments are similar in SRB, because OL generally performs well in this basin (Figure 6k and

500 p) and the SWE increment in the northern SRB by different DA experiments contributes only a

501 small proportion of the water to the streamflow.

502 Kumar et al. (2014) also found notable degradations in streamflow over UCRB by

503 assimilating a blended in situ-satellite SD product, which employs in situ measurements from the

504 Global Historical Climatology Network (GHCN) and satellite retrievals from SMMR, Special

505 Sensor Microwave Imager (SSM/I), and AMSR-E. They concluded that in situ bias correction of

506 the PMW SD retrievals remains insufficient to provide subsequent skill improvements in

507 streamflow simulation in this heterogeneous basin due to the low representativeness of the in situ

508 observations. Liu et al. (2015) demonstrated that using SNOTEL observations in the blending of

509 in situ and PMW SWE data without considering terrain aspect leads to substantial overestimation

510 in snow and thus streamflow in UCRB. We conclude that although incorporating terrain aspect in

511 the blending process can improve the SWE estimates of the blended product (Gan et al., 2021), the

512 improvement of streamflow by assimilating this blended product is still not promising in

513 heterogeneous basins such as the UCRB, due to the relatively poor performance of the model, low

514 representativeness of the in situ observations and large uncertainties of the PMW retrievals.
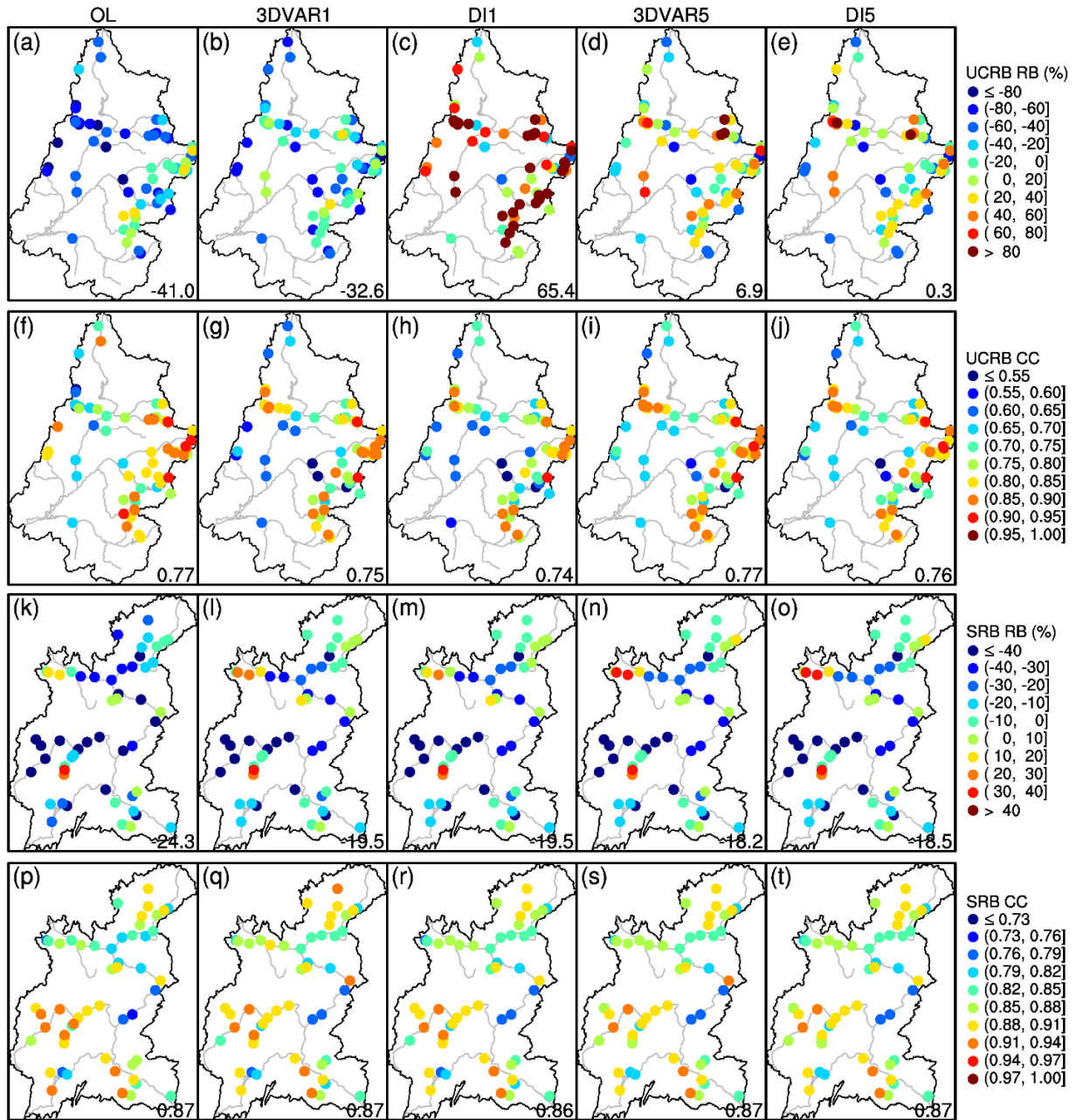
Figure 6. Spatial distributions of relative bias (RB) and correlation coefficient (CC) of the daily streamflow discharge from the OL (first column), 3DVAR1 (second column), DI1 (third column), 3DVAR5 (fourth column), and DI5 (fifth column) experiments against USGS observations in the water years 2017–2019 for selected gauges in UCRB and SRB. The number on the bottom right corner of each subfigure presents the average value.

4.3. Concurrent comparison of SWE and streamflow

We examine concurrent changes in SWE and streamflow simulation accuracy (against SNODAS SWE analysis and USGS streamflow observations, respectively) for 67 UCRB subbasins and 54 SRB subbasins after the application of DA to identify the characteristics of the changes and the possible causes for the improvements/deteriorations of model performance.

4.3.1. Which DA experiment performs best?

To gain more insight into the effects of DA on SWE and streamflow simulations, we compare different DA experiments with OL experiment on the subbasin scale. Table 3 summarizes the percentage of subbasins with improved statistics as compared to OL. Generally, more subbasins experience improvements in SWE simulation than in streamflow simulation except for the UCRB's 3DVAR1 case, indicating that the improved SWE does not always translate into improved streamflow. This is a quite common feature that has been reported not only in SD/SWE assimilation (Kumar et al., 2014; Liu et al., 2015) but also in the assimilation of other variables such as soil moisture (Yan and Moradkhani, 2016) and terrestrial water storage (Tangdamrongsub et al., 2015), due to the differing streamflow responses in different subbasins to the redistribution of water mass. Meanwhile, more SRB subbasins see improvements than do UCRB subbasins for both SWE and streamflow simulations in all the DA experiments, although the degree of improvement is more pronounced for UCRB subbasins due to the relatively poorer performance of the OL simulation. Moreover, although DI outperforms 3DVAR with the same assimilation frequency for SWE simulation in UCRB, it underperforms 3DVAR for streamflow simulation. This is because the direct replacement of model states with observations (i.e., blended SWE data) by DI may introduce physically unrealistic changes in model states (e.g., the violation of mass conservation), while 3DVAR allows the physical relationship between model states to be better

545　maintained through assimilation (Magnusson et al., 2017). For 3DVAR, reducing assimilation

546　frequency from daily to every 5 days generally yields improved streamflow simulation because

547　the higher frequency leads to more severe overestimation of SWE and thus streamflow in more

548　subbasins. We therefore focus on the 3DVAR scheme with the assimilation frequency set to every

549　5 days (3DVAR5) for both basins in subsequent analyses.

550　**Table 3.** Percentage of subbasins with improved statistics for SWE and streamflow simulations
551　in UCRB and SRB as compared to OL.

Basin	Case	SWE		Streamflow	
		Subbasins with improved |RB| (%)	Subbasins with improved CC (%)	Subbasins with improved |RB| (%)	Subbasins with improved CC (%)
UCRB	3DVAR1	46.3	44.8	65.7	29.9
	DI1	77.6	85.1	37.3	20.9
	3DVAR5	68.7	68.7	62.7	38.8
	DI5	80.6	74.6	64.2	28.4
SRB	3DVAR1	96.3	87.0	74.1	66.7
	DI1	87.0	88.9	70.4	64.8
	3DVAR5	90.7	96.3	75.9	70.4
	DI5	90.7	87.0	75.9	70.4

552

4.3.2.　How does DA improve OL?

554　　To determine how does DA influence SWE and streamflow in different subbasins, we

555　examine the changes of RB from OL to 3DVAR5. Figure 7 compares the RB of SWE and

556　streamflow for 3DVAR5 against OL experiments at all selected subbasins in UCRB and SRB. OL

557　underestimates SWE and streamflow for 98.5% and 85.1% of the UCRB subbasins (points in the

558　$y < 0$ region of Figure 7a and b), respectively, and for 100% and 83.3% of the SRB subbasins

559　(points in the $y < 0$ region of Figure 7c and d), respectively. The assimilation of the blended SWE

560　product by 3DVAR5 reduces the percentage of subbasins with underestimated SWE and

561　streamflow to 55.2% and 41.8% for UCRB (points in the $x < 0$ region of Figure 7a and b),

562 respectively, and to 77.8% and 74.1% for SRB (points in the x < 0 region of Figure 7c and d),

563 respectively. The increased SWE and streamflow by 3DVAR5 lead to improved SWE and

564 streamflow for 68.7% and 62.7% of the UCRB subbasins (points in gray regions of Figure 7a and

565 b), respectively, and for 90.7% and 75.9% of the SRB subbasins (points in gray regions of Figure

566 7c and d), respectively. The relatively lower percentage of improved subbasins in UCRB is due to

567 the fact that 3DVAR5 yields overestimated SWE and streamflow in more UCRB subbasins, which

568 results in larger |RB| as compared to the OL (points in the right white region of Figure 7a and b).

569 Specifically, 3DVAR5 increases RB from a negative value to a positive one with a larger absolute

570 value for SWE and streamflow in 22.4% and 19.4% of the UCRB subbasins (points in the lower-

571 right white region of Figure 7a and b), respectively, and in 9.3% and 5.6% of the SRB subbasins

572 (points in the lower-right white region of Figure 7c and d), respectively. Meanwhile, it also

573 increases RB from a smaller positive value to a larger one for SWE and streamflow in 1.5% and

574 11.9% of the UCRB subbasins (points in the upper-right white region of Figure 7a and b),

575 respectively, and in 0% and 13% of the SRB subbasins (points in the upper-right white region of

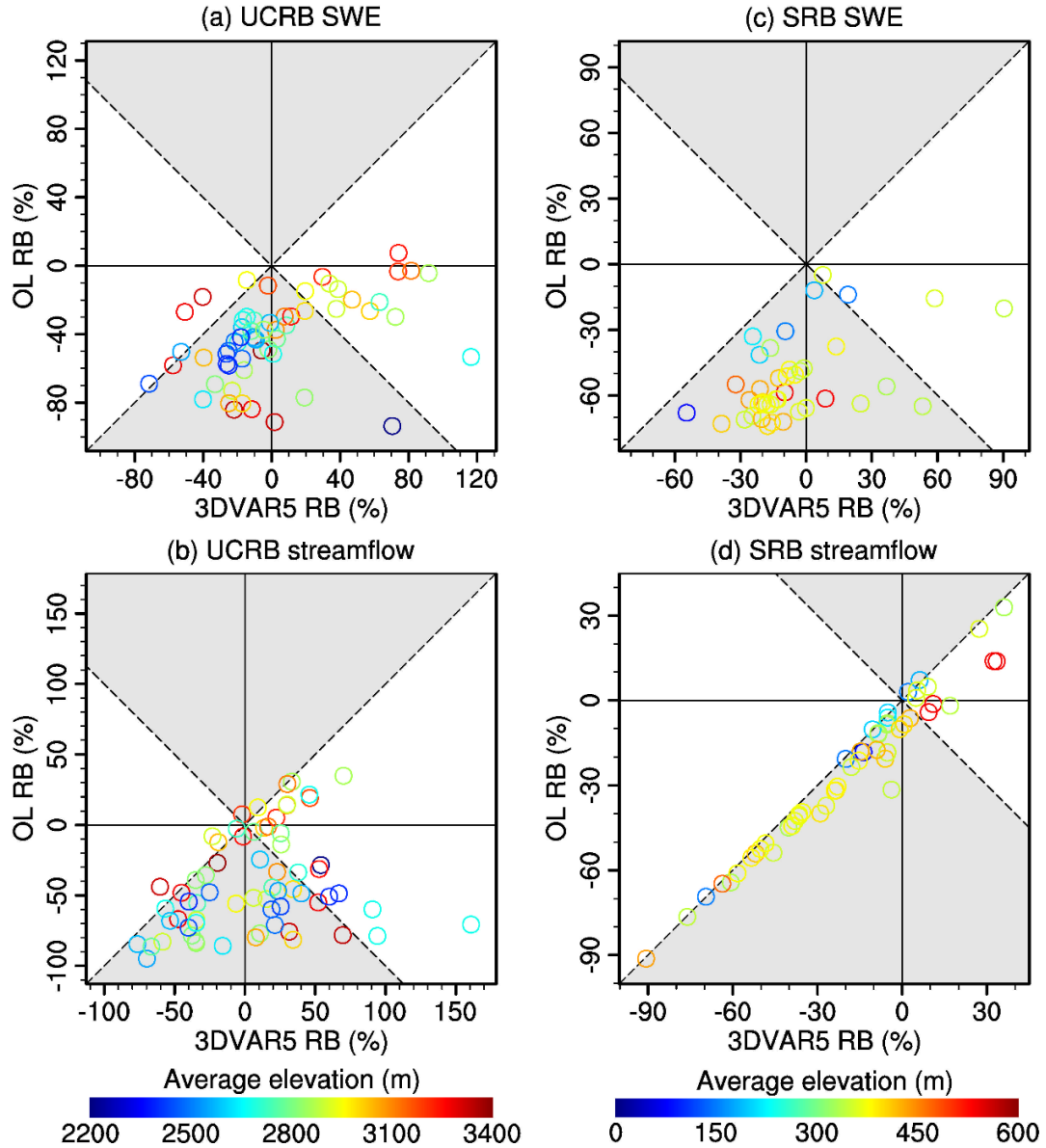576 Figure 7c and d), respectively.

Figure 7. Scatterplots of relative bias (RB) of (a) UCRB SWE, (b) UCRB streamflow, (c) SRB SWE, and (d) SRB streamflow relative to the reference data for 3DVAR5 against OL experiments at all selected subbasins. Each point corresponds to an individual subbasin with the color represents its average elevation. For each subfigure, two gray dashed lines (y = x and y = −x) are plotted to divide the panel into four regions, in which the two gray regions represent |x| < |y|. Points in the gray regions indicate that DA performs better than OL for those subbasins. Negative values indicate model underestimation as compared to the reference data.

4.3.3. How does SWE influence streamflow?

We analyze the relationship between SWE and streamflow simulations by calculating the percentages of subbasins in the following four categories: 1) improved SWE + improved streamflow, 2) degraded SWE + improved streamflow, 3) improved SWE + degraded streamflow, and 4) degraded SWE + degraded streamflow. Figure 8 shows the scatterplots of the differences in |RB| and CC between 3DVAR5 and OL experiments for SWE and streamflow simulations in UCRB and SRB. As compared to the OL, 47.8% of the UCRB subbasins have improved |RB| (R3 of Figure 8a) and 29.9% of them have improved CC (R1 of Figure 8b) for both SWE and streamflow by 3DVAR5; 70.4% of the SRB subbasins have improved |RB| (R3 of Figure 8c) and 68.5% of them have improved CC (R1 of Figure 8d) for both SWE and streamflow by 3DVAR5. More interestingly, |RB| of 14.9% of the UCRB subbasins (R4 of Figure 8a) and CC of 9.0% of the UCRB subbasins (R2 of Figure 8b), as well as |RB| of 5.6% of the SRB subbasins (R4 of Figure 8c) and CC of 1.9% of the SRB subbasins (R2 of Figure 8d) are improved for streamflow simulation by 3DVAR5, even though the SWE simulation is degraded for them. By contrast, 3DVAR5 improves SWE but degrades streamflow for |RB| of 20.9% of the UCRB subbasins (R2 of Figure 8a) and for CC of 38.8% of the UCRB subbasins (R4 of Figure 8b); and for |RB| of 20.4% of the SRB subbasins (R2 of Figure 8c) and for CC of 27.8% of the SRB subbasins (R4 of Figure 8d). One possible reason is that the calibrated/default parameters for streamflow simulation may compensate for SWE discrepancies, thus if SWE are improved by DA there could be degradations in streamflow. Furthermore, 3DVAR5 degrades SWE and then streamflow for |RB| of 16.4% of the UCRB subbasins (R1 of Figure 8a) and for CC of 22.4% of the UCRB subbasins (R3 of Figure 8b) as well as for |RB| of 3.7% of the SRB subbasins (R1 of Figure 8c) and for CC of 1.9% of the SRB subbasins (R3 of Figure 8d). It is observable that more subbasins experience improvements

609   for both SWE and streamflow simulations in both basins. In addition, the percentage of subbasins

610   with improved SWE and streamflow is higher for SRB than for UCRB, despite the degree of

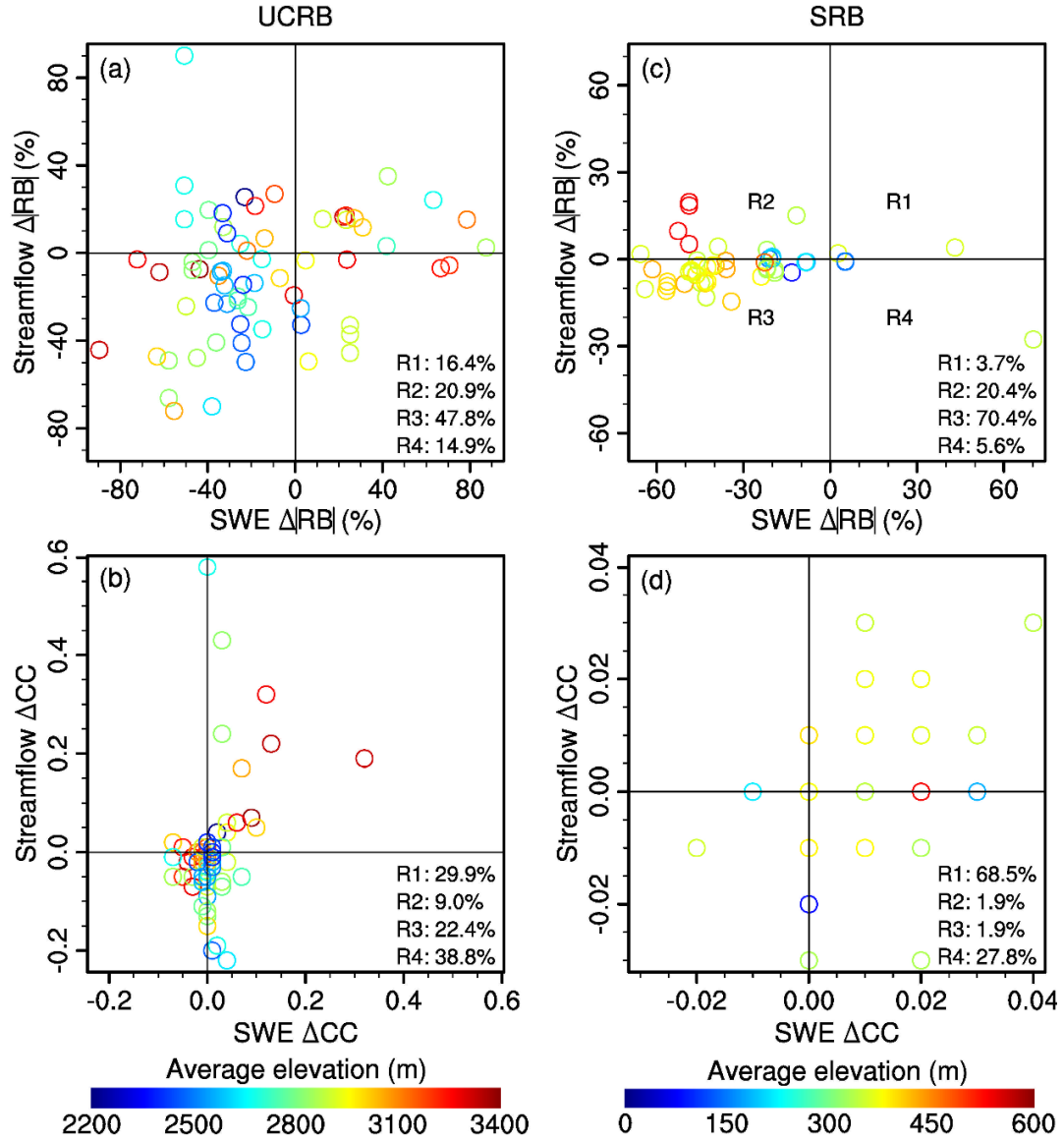611   improvement (especially the CC) is smaller for the former.

612
613   **Figure 8.** Scatterplots of the differences of the statistics (absolute relative bias |RB| and correlation
614   coefficient CC) between 3DVAR5 and OL experiments for SWE against streamflow simulations
615   in UCRB (left column) and SRB (right column). Each point corresponds to an individual subbasin
616   with the color represents its average elevation. For each subfigure, two lines (x = 0 and y = 0) are
617   plotted to divide the panel into four regions R1 (x ≥ 0, y ≥ 0), R2 (x < 0, y ≥ 0), R3 (x < 0, y < 0),
618   and R4 (x ≥ 0, y < 0). The negative values of Δ|RB| and the positive values of ΔCC indicate
619   improvement of 3DVAR5 as compared to OL. On the lower right corner of each subfigure shows
620   the percentages of subbasins locate in the four regions.

621

4.3.4. What are the reasons for the improvements/deteriorations?

Figure 9 and Figure 10 compare the time series of spatial-averaged daily SWE and outlet streamflow for a pair of chosen subbasins within UCRB and SRB (see Section 2.1), respectively. SWE and streamflow are underestimated by OL simulation in the four selected subbasins, and 3DVAR5 significantly improves the underestimated SWE, which reduces the |RB| by 63.2%, 33.2%, 34.2%, and 48.0% for them (Figure 9a and b and Figure 10a and b), respectively. However, although it corrects the streamflow bias during the ablation period in both SRB subbasins (Figure 10), the streamflow remains underestimated in the whole period, especially for the larger subbasin (Figure 10b). This systematic streamflow bias in SRB is not caused by SWE bias and it could be corrected by model calibration. 3DVAR5 generally overestimates streamflow for both UCRB subbasins (Figure 9), but it improves the streamflow simulation (reduces |RB| by 47.2%) for the smaller subbasin as compared to the OL (Figure 9a). Streamflow observations start increasing around March, peak in June, and return to base flow levels in August, but the 3DVAR5 simulations exhibit a longer period of high flow and lower base flow in UCRB subbasins. It is also observed that the timing of all major peaks is well captured for the small subbasin (Figure 9a) whereas it exhibits obvious deviation for the large subbasin (Figure 9b) in UCRB after DA. Additionally, 3DVAR5 results in earlier peak flow timing and larger peak flow magnitude than the observed streamflow for the large UCRB subbasin (Figure 9b).
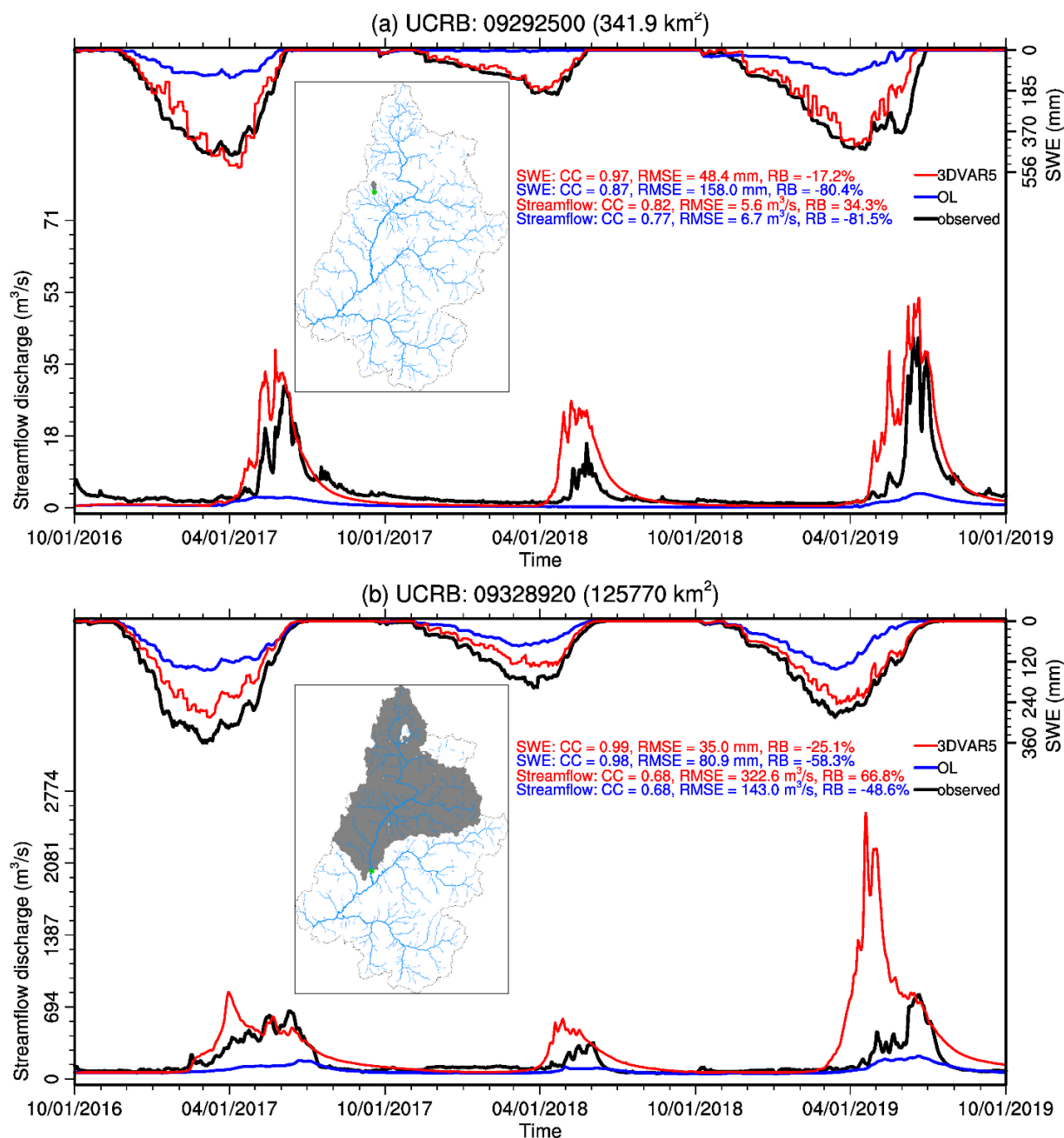
Figure 9. Time series of the daily SWE and streamflow discharge for two representative subbasins in UCRB. The map on each subfigure shows the locations of the subbasin and corresponding outlet. CC, BIAS, and RB represent the correlation coefficient, bias, and relative bias of model simulations against reference data (i.e., SNODAS SWE analysis and USGS streamflow observations), respectively.
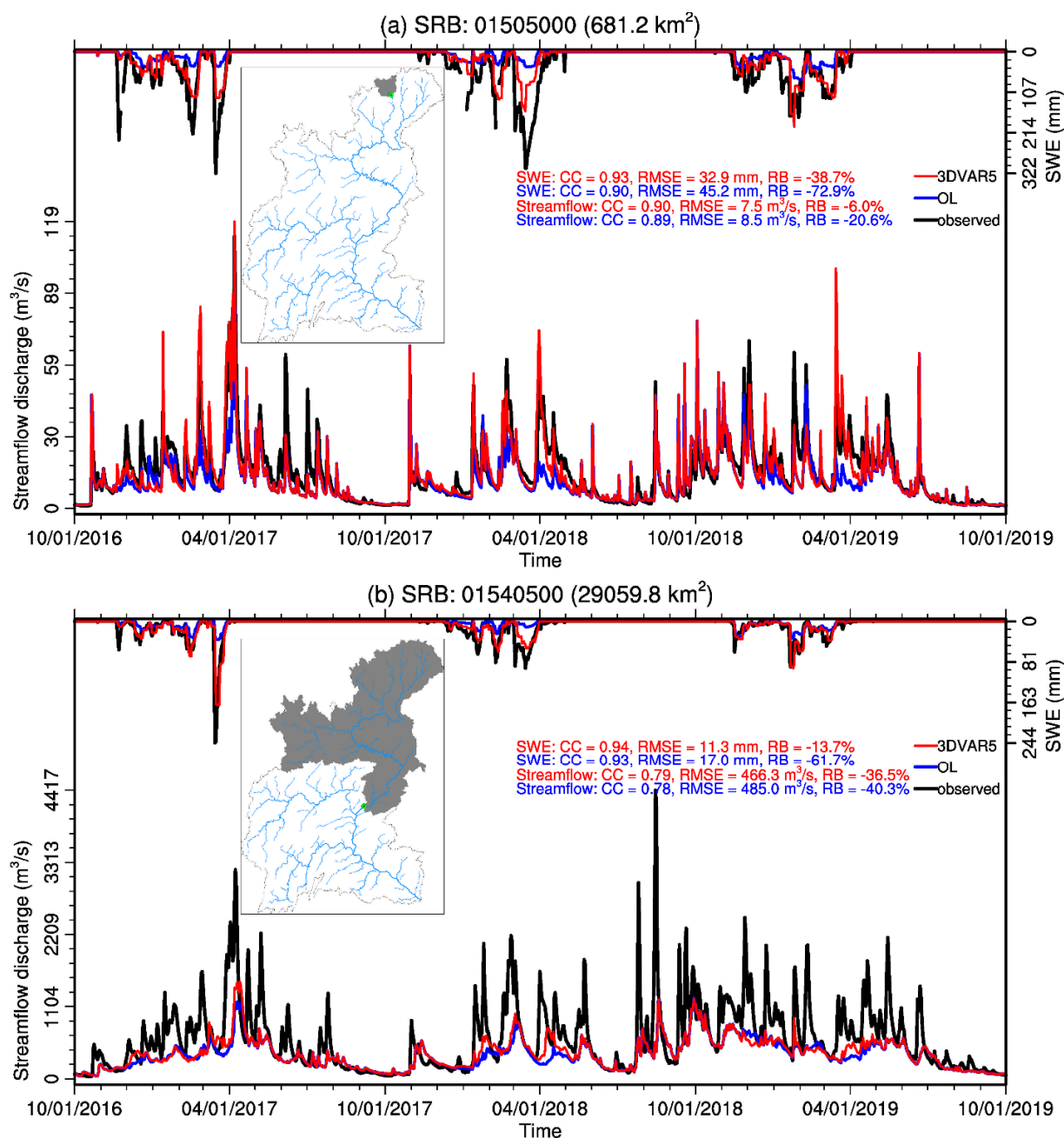
35

Figure 10. Time series of the daily SWE and streamflow discharge for two representative subbasins in SRB. The map on each subfigure shows the locations of the subbasin and corresponding outlet. CC, BIAS, and RB represent the correlation coefficient, bias, and relative bias of model simulations against reference data (i.e., SNODAS SWE analysis and USGS streamflow observations), respectively.

36

654   A further examination of all 67 UCRB subbasins shows that 55 of them have earlier peak

655   flows in the OL simulation (i.e., with modeled peaks preceding the observed ones), among which

656   11 are calibrated subbasins and the other 44 are uncalibrated subbasins. 3DVAR5 slightly mitigates

657   the timing error—it helps reduce the number of subbasins with earlier peak flow timing from 55

658   to 48, of which 40 are non-calibrated subbasins, 7 are calibrated subbasins that also have earlier

659   peak flows in the OL simulation, and only 1 is calibrated subbasin that does not have earlier peak

660   flows in the OL simulation (see Table S1). This illustrates that recalibration of the model is

661   necessary for some of the UCRB subbasins. Meanwhile, although the timing of peak flows is well

662   captured for all SRB subbasins, the magnitude is underestimated by over 40% for 17 SRB

663   subbasins in the OL simulation. Even though 3DVAR5 alleviates the underestimation of the

664   magnitude for most of the SRB subbasins, there are still 11 subbasins that underestimate the

665   magnitude by over 40% (see Table S1). Again, this indicates that recalibration of the model for

666   some of the SRB subbasins is also necessary despite the model has good performance in most SRB

667   subbasins.

668   The inconsistency between 3DVAR5 simulations and the USGS observations in UCRB

669   subbasins can be partly explained by the fact that anthropogenic activities such as reservoir

670   operation (e.g., Fontenelle and Flaming Gorge Dams in the Green River), irrigation withdrawal,

671   and streamflow diversion in this basin greatly alter the natural flow regime, that is, reduce total

672   annual runoff, increase base flow, decrease peak flow magnitude, and shift peak flow timing. The

673   earlier peak flow timing of 3DVAR5 simulations may be attributed to the fact that much of the

674   snow incrementally ingested by DA enters the model prior to the melt season. As NWM was

675   calibrated using the snowpack without accounting for this addition (or even uncalibrated for many

676   UCRB subbasins and most SRB subbasins), it tends to create an amplified streamflow peak by

677 rapidly melting this added snow right at the onset of the melt season due to the low snow albedo

678 as mentioned earlier. This induces a phase shift in the modeled seasonal streamflow, and also

679 contributes to the large increase in peak flow (Barnhart et al., 2016). This suggests a necessity to

680 calibrate the SWE before the calibration of streamflow in this snow-dominated basin.

681 **5. Summary and conclusions**

682   This study investigates the potential of assimilating a blended in situ-satellite SWE product

683 for improving snow and streamflow simulations of the NWM in two US river basins—UCRB with

684 seasonal snow and SRB with ephemeral snow. This blended SWE product is assimilated into the

685 operational NWM through a newly developed snow assimilation strategy. Different assimilation

686 methods (3DVAR and DI) and assimilation frequencies (daily and every 5 days) are tested to

687 examine their influence on assimilation effect.

688   The OL simulation underestimates SWE in both basins as compared to the SNODAS analysis

689 although they have high correlation. The negative bias of SWE thus contributes to the

690 underestimated streamflow in both basins. Assimilating the blended SWE product considerably

691 alleviates the underestimated SWE throughout the snow seasons in both basins, with more

692 reasonable temporal variation and spatial distribution. Overall, 3DVAR with a every 5 days

693 assimilation frequency (3DVAR5) and DI with a daily assimilation frequency (DI1) produce

694 spatial-averaged time series in closer agreement with the SNODAS analysis than 3DVAR with a

695 daily assimilation frequency (3DVAR1) and DI with a every 5 days assimilation frequency (DI5)

696 in UCRB. Comparatively, all DA experiments (3DVAR1, DI1, 3DVAR5, and DI5) perform

697 similarly in SRB. While 3DVAR and DI perform similarly in SRB due to the short accumulation-

698 ablation processes of the ephemeral snow, the former produces larger SWE than the latter with a

699 higher assimilation frequency in UCRB due to the sequential ingestion of the continuously

700   increasing blended SWE product. Moreover, 3DVAR with a higher assimilation frequency (i.e.,

701   3DVAR1) generates more heterogeneous spatial pattern of SWE in UCRB due to the cumulative

702   effect of sequentially imposing spatially heterogeneous blended SWE product.

703   The assimilation of the blended SWE product mitigates the underestimation of streamflow in

704   NWM OL simulations for both basins. However, it largely overestimates streamflow for some of

705   the UCRB subbasins due to the overestimated SWE. Besides, it has more obvious influences on

706   streamflow for UCRB than for SRB. This is because snowfall is the main source of precipitation

707   in UCRB and the change of SWE significantly affects not only surface runoff but also subsurface

708   runoff, evapotranspiration, and soil moisture in this basin, and these mechanisms are difficult to

709   capture by the model. However, the percentage of subbasins with improved streamflow is smaller

710   for UCRB than for SRB due to the relatively poorer model performance and the larger uncertainty

711   of the blended SWE product in the former basin. Generally, fewer subbasins experience improved

712   streamflow simulation than SWE simulation, indicating that improved SWE does not always

713   translate into improved streamflow. 3DVAR outperforms DI with the same assimilation frequency

714   for streamflow simulation in most selected UCRB and SRB subbasins, despite its relatively worse

715   performance for SWE simulation in most UCRB subbasins when with a daily assimilation

716   frequency. 3DVAR with a lower assimilation frequency (i.e., 3DVAR5) performs better than that

717   with a higher assimilation frequency (i.e., 3DVAR1) for streamflow simulation in both basins.

718   While the snow assimilation strategy proposed in this paper is overall effective in mitigating

719   the biases in snowpack, and, to a lesser extent, streamflow, its effect is strongly dependent upon

720   the types of snowpack and differential assimilation methods and frequencies. Besides, the blended

721   SWE product has relatively large biases in heterogeneous regions such as the UCRB due to limited

722   representativeness of the in situ network and the low reliability of the PMW retrievals. This

blended product may be improved by incorporating observations from other emerging platforms such as the Sentinel-1 C-band synthetic aperture radar (Lievens et al., 2019) and airborne lidar (Painter et al., 2016), and the improvement of the blended SWE product would eventually benefit streamflow simulation. Moreover, neither 3DVAR nor DI provides any estimate of predictive uncertainty, while the uncertainties from precipitation and air temperature need to be quantified since they are the main drivers of SWE and streamflow dynamics. SWE can also be influenced by many processes such as the snow albedo and below-canopy turbulence and radiation transfer parameterizations. Therefore, it will be useful to explore the assimilation of snow albedo and SWE jointly for improving snow and terrestrial water budget estimates (Kumar et al., 2020). Furthermore, NWM performs relatively poorly in UCRB and snow DA of the NWM may increase the uncertainty since it redistributes water in different hydrologic processes. As such, recalibration of the NWM or application of the DA techniques to improve the estimation of not only the state variables but also the influencing parameters may be a necessity. Finally, much remains to be done to assess the potential of the blended product and assimilation strategy for other geographic regions with disparate ablation processes. These will be left in future efforts.

Appendix A. Snow physics

Noah-MP snow model is an energy and mass balance model that features an up to 3-layer representation of snowpack (Yang and Niu, 2003). More detailed information can be found in Yang et al. (2011). We give a brief description of the snow physics adopted in the NWM below.

a. Snowfall

The precipitation rate P (mm s^{-1}) is partitioned into rainfall rate P_r (mm s^{-1}) and snowfall rate P_s (mm s^{-1}) following Jordan (1991).

$$P_s = \begin{cases} 0, & T_{sfc} > T_{frz} + 2.5 \\ 0.6P, & T_{frz} + 2 < T_{sfc} \leq T_{frz} + 2.5 \\ P[1 - (-54.632 + 0.2T_{sfc})], & T_{frz} + 0.5 < T_{sfc} \leq T_{frz} + 2 \\ P, & T_{sfc} \leq T_{frz} + 0.5 \end{cases} \qquad \text{(A.1)}$$

where T_{sfc} is the surface air temperature; and T_{frz} is the freezing/melting temperature (273.15 K).

Snowfall is intercepted by the vegetation canopy using a snow interception model (Niu and Yang, 2004). The snowfall rate at the ground surface $P_{s,g}$ (mm s^{-1}) is then calculated by

$$P_{s,g} = P_{s,drip} + P_{s,throu} \qquad \text{(A.2)}$$

where $P_{s,drip}$ (mm s^{-1}) is the drip rate of snow; and $P_{s,throu}$ (mm s^{-1}) is the through-fall rate of snow.

b. Snow depth

Snow depth h_s (mm) is calculated by

$$h_s^t = h_s^{t-1} + \frac{P_{s,g}}{\rho_{sf}} dt \qquad \text{(A.3)}$$

where $P_{s,g}$ is the snowfall rate at the ground surface (mm s^{-1}); dt is the timestep (s); and ρ_{sf} is the bulk density of the snowfall (kg m^{-3}) that can be calculated following Hedstrom and Pomeroy (1998)

765
$$\rho_{sf} = \min\left(120, 67.92 + 51.25e^{\frac{T_{sfc}-T_{frz}}{2.59}}\right) \qquad \text{(A.4)}$$

766   where T_{sfc} and T_{frz} were stated above.

c. Snow layer

768   Snowpack can be divided by up to three layers depending on the snow depth h_s (Niu et al.,

769   2011). When $h_s < 0.025$ m, no snow layer exists, and the snowpack is combined with the topsoil

770   layer. When $0.025 \leq h_s \leq 0.05$ m, a single layer is created with snow layer thickness $\Delta Z_0 = h_s$

771   m. When $0.05 < h_s \leq 0.1$ m, two snow layers are formed with snow layer thickness $\Delta Z_{-1} =$

772   $\Delta Z_0 = h_s/2$ m. When $0.1 < h_s \leq 0.25$ m, two snow layers are again formed, but the two-layer

773   thicknesses are $\Delta Z_{-1} = 0.05$ m and $\Delta Z_0 = h_s - 0.05$ m. When $0.25 < h_s \leq 0.45$ m, three layers

774   are created with $\Delta Z_{-2} = 0.05$ m and $\Delta Z_{-1} = \Delta Z_0 = (h_s - 0.05)/2$ m. When $h_s > 0.45$ m, three

775   layers are again created, but the three-layer thicknesses are $\Delta Z_{-2} = 0.05$ m, $\Delta Z_{-1} = 0.2$ m, and

776   $\Delta Z_0 = h_s - 0.25$ m.

d. Snow cover

778   The snow cover fraction is parameterized as (Niu and Yang, 2007)

779
$$f_s = \tan\left(\frac{h_s}{2.5Z_{0,g}(\rho_s/\rho_{new})^m}\right) \qquad \text{(A.5)}$$

780   Where h_s is the snow depth; $Z_{0,g}$ is the ground roughness length (here $Z_{0g} = 0.002$ m); ρ_s is the

781   bulk density of the snowpack (kg m^{-3}); ρ_{new} is the fresh snow density (here $\rho_{new} = 100$ kg m^{-3});

782   and m is the melting factor determining the snow cover fraction–snow depth curves in the melting

783   season.

784 **e. Snow albedo**

785   The snow albedo scheme adopted in NWM is from Biosphere-Atmosphere Transfer Scheme

786 (BATS; Yang et al., 1997). It calculates snow albedo for both visible ("*VIS*") and near-infrared

787 ("*NIR*") bands under both direct ("*dir*") and diffuse ("*dif*") radiations. For the diffuse radiation,

788
$$\begin{cases} \alpha_s^{dif,VIS} = 0.95\big(1 - 0.2 f_{age}\big) \\ \alpha_s^{dif,NIR} = 0.65\big(1 - 0.5 f_{age}\big) \end{cases} \tag{A.6}$$

789 where f_{age} is the snow age function. For the direct radiation,

790
$$\begin{cases} \alpha_s^{dir,VIS} = \alpha_s^{dif,VIS} + 0.4 f_Z\big(1 - \alpha_s^{dif,VIS}\big) \\ \alpha_s^{dir,NIR} = \alpha_s^{dif,NIR} + 0.4 f_Z\big(1 - \alpha_s^{dif,NIR}\big) \end{cases} \tag{A.7}$$

791 where f_Z is a factor that accounts for the impact of solar zenith angle Z.

792 **f. Snow temperature**

793   Snow skin temperatures for the vegetated ground ($T_{g,v}$, K) and bare ground ($T_{g,b}$, K) are

794 obtained by iteratively solving the snow surface energy balance equations, respectively

795
$$F_{veg} S_g = F_{veg}\left(L_{g,v}\big(T_{g,v}\big) + H_{g,v}\big(T_{g,v}\big) + \lambda E_{g,v}\big(T_{g,v}\big) + G_{g,v}\big(T_{g,v}\big) \right) \tag{A.8}$$

796
$$\big(1 - F_{veg}\big) S_g = \big(1 - F_{veg}\big)\left(L_{g,b}\big(T_{g,b}\big) + H_{g,b}\big(T_{g,b}\big) + \lambda E_{g,b}\big(T_{g,b}\big) + G_{g,b}\big(T_{g,b}\big) \right) \tag{A.9}$$

797 where F_{veg} is the green vegetation fraction (dimensionless); S is the net solar radiation (W m^{-2}); L

798 is the net longwave radiation (W m^{-2}); H is the sensible heat (W m^{-2}); λE is the latent heat (W

799 m^{-2}); G is the ground heat fluxes (W m^{-2}); and the subscripts "*g*", "*g,v*" and "*g,b*" refer to ground,

800 vegetated ground, and bare ground, respectively.

801   The temperature of the snow and soil layers are solved together through one tridiagonal matrix

802 with its dimension varying with the total number of snow and soil layers (Niu et al., 2011). Snow

803 melting occurs when a snow layer's ice content exists and the snow temperature is above 273.15

804 K.

805 **g. Snow water**

806   The temporal change of SWE is balanced by the input snowfall, and output snow sublimation

807 and snowmelt as

808 $$\frac{dW_s}{dt} = P_{s,g} - E_{s,g} - M_{s,g} \tag{A.10}$$

809 where W_s is the SWE (mm); $P_{s,g}$ is the snowfall rate at the ground (mm s^{-1}), which was introduced

810 above. $E_{s,g}$ is the snow sublimation rate (mm s^{-1})

811 $$E_{s,g} = \min\left(E_g, \frac{SWE}{dt}\right) \tag{A.11}$$

812 where E_g is the ground surface evaporation rate (mm s^{-1}). $M_{s,g}$ is the snowmelt rate (mm s^{-1})

813 $$M_{s,g} = \frac{1}{L_f}\left(S_g + L_g - H_g - \lambda E_g - G_g\right) \tag{A.12}$$

814 where L_f is the latent heat of fusion (0.3336×10^6 J kg^{-1}); and S, L, H, λE, G and the subscript "g"

815 were stated above.

816 **Appendix B. Supplementary data**

817 Tables S1–S2.

818 Figures S1–S2.

819 **References**

820 Anderson, B.T., 2011. Spatial Distribution and Evolution of a Seasonal Snowpack in Complex

821   Terrain: An Evaluation of the SNODAS Modeling Product. Master of Science, Boise State

822   University, Boise, Idaho.

823 Anderson, E.A., 1973. National Weather Service river forecast system—snow accumulation and

824   ablation model. NOAA, Silver Spring, Maryland.

825 Andreadis, K.M., Lettenmaier, D.P., 2006. Assimilating remotely sensed snow observations into

826   a   macroscale   hydrology   model.   Adv.   Water   Resour.   29   (6),   872–886.

827   https://doi.org/10.1016/j.advwatres.2005.08.004.

828 Andreadis, K.M., Liang, D., Tsang, L., Lettenmaier, D.P., Josberger, E.G., 2008. Characterization

829   of errors in a coupled snow hydrology–microwave emission model. J. Hydrometeorol. 9 (1),

830   149–164. https://doi.org/10.1175/2007JHM885.1.

831 Arsenault, K.R., Nearing, G.S., Wang, S., Yatheendradas, S., Peters-Lidard, C.D., 2018. Parameter

832   sensitivity of the Noah-MP land surface model with dynamic vegetation. J. Hydrometeorol.

833   19 (5), 815–830. https://doi.org/10.1175/jhm-d-17-0205.1.

834 Barlage, M., Chen, F., Tewari, M., Ikeda, K., Gochis, D., Dudhia, J., Rasmussen, R., Livneh, B.,

835   Ek, M., Mitchell, K., 2010. Noah land surface model modifications to improve snowpack

836   prediction in the Colorado Rocky Mountains. J. Geophys. Res. Atmos. 115 (D22).

837   https://doi.org/https://doi.org/10.1029/2009JD013470.

838   Barnhart, T.B., Molotch, N.P., Livneh, B., Harpold, A.A., Knowles, J.F., Schneider, D., 2016.

839   Snowmelt rate dictates streamflow. Geophys. Res. Lett. 43 (15), 8006–8016.

840   https://doi.org/10.1002/2016GL069690.

841   Bouttier, F., Courtier, P., 2002. Data assimilation concepts and methods. ECMWF, Reading, UK.

842   Carroll, T., Cline, D., Fall, G., Nilsson, A., Li, L., Rost, A., 2001. NOHRSC operations and the

843   simulation of snow cover properties for the coterminous US, in: Proceedings of the 69th

844   Annual Western Snow Conference, Sun Valley, Idaho, pp. 1–14.

845   Chen, F., Barlage, M., Tewari, M., Rasmussen, R., Jin, J., Lettenmaier, D., Livneh, B., Lin, C.,

846   Miguez-Macho, G., Niu, G.-Y., Wen, L., Yang, Z.-L., 2014. Modeling seasonal snowpack

847   evolution in the complex terrain and forested Colorado Headwaters region: A model

848   intercomparison study. J. Geophys. Res. Atmos. 119, 13795–13819.

849   https://doi.org/10.1002/2014JD022167.

850   Clark, M.P., Slater, A.G., Barrett, A.P., Hay, L.E., McCabe, G.J., Rajagopalan, B., Leavesley,

851   G.H., 2006. Assimilation of snow covered area information into hydrologic and land-surface

852   models. Adv. Water Resour. 29 (8), 1209–1221.

853   https://doi.org/10.1016/j.advwatres.2005.10.001.

854   Clow, D.W., Nanus, L., Verdin, K.L., Schmidt, J., 2012. Evaluation of SNODAS snow depth and

855   snow water equivalent estimates for the Colorado Rocky Mountains, USA. Hydrol. Process.

856   26 (17), 2583–2591. https://doi.org/10.1002/hyp.9385.

857   Courtier, P., Thépaut, J.N., Hollingsworth, A., 1994. A strategy for operational implementation of

858   4D-Var, using an incremental approach. Q. J. Roy. Meteor. Soc. 120 (519), 1367–1387.

859   https://doi.org/10.1002/qj.49712051912.

860   De Lannoy, G.J.M., Reichle, R.H., Arsenault, K.R., Houser, P.R., Kumar, S., Verhoest, N.E.C.,

861   Pauwels, V.R.N., 2012. Multiscale assimilation of Advanced Microwave Scanning

862   Radiometer–EOS snow water equivalent and Moderate Resolution Imaging

863   Spectroradiometer snow cover fraction observations in northern Colorado. Water Resour. Res.

864   48 (1), W01522. https://doi.org/10.1029/2011WR010588.

865   Del Moral, P., 1996. Nonlinear filtering: Interacting particle resolution. Markov Process. Relat. 2

866   (4), 555–580.

867   Dietz, A.J., Kuenzer, C., Gessner, U., Dech, S., 2012. Remote sensing of snow – a review of

868   available methods. Int. J. Remote Sens. 33 (13), 4094–4134.

869   https://doi.org/10.1080/01431161.2011.640964.

870   Dong, C., 2018. Remote sensing, hydrological modeling and in situ observations in snow cover

871   research: A review. J. Hydrol. 561, 573–583. https://doi.org/10.1016/j.jhydrol.2018.04.027.

872   Dong, J., Walker, J.P., Houser, P.R., Sun, C., 2007. Scanning multichannel microwave radiometer

873   snow water equivalent assimilation. J. Geophys. Res. Atmos. 112 (D7), D07108.

874   https://doi.org/10.1029/2006JD007209.

875   Dozier, J., Bair, E.H., Davis, R.E., 2016. Estimating the spatial distribution of snow water

876   equivalent in the world's mountains. WIREs Water 3 (3), 461–474.

877   https://doi.org/10.1002/wat2.1140.

878   Durand, M., Margulis, S.A., 2007. Correcting first-order errors in snow water equivalent estimates

879   using a multifrequency, multiscale radiometric data assimilation scheme. J. Geophys. Res.

880   Atmos. 112 (D13), D13121. https://doi.org/10.1029/2006JD008067.

881   Durand, M., Kim, E.J., Margulis, S.A., 2008. Quantifying uncertainty in modeling snow

882   microwave radiance for a mountain snowpack at the point-scale, including stratigraphic

883   effects. IEEE T. Geosci. Remote 46 (6), 1753–1767.

884   https://doi.org/10.1109/TGRS.2008.916221.

885   Essery, R., Morin, S., Lejeune, Y., B Ménard, C., 2013. A comparison of 1701 snow models using

886   observations from an alpine site. Adv. Water Resour. 55, 131–148.

887   https://doi.org/10.1016/j.advwatres.2012.07.013.

888   Evensen, G., 1994. Sequential data assimilation with a nonlinear quasi-geostrophic model using

889   Monte Carlo methods to forecast error statistics. J. Geophys. Res. Oceans 99 (C5), 10143–

890   10162. https://doi.org/10.1029/94JC00572.

891   Franz, K.J., Hogue, T.S., Sorooshian, S., 2008. Operational snow modeling: Addressing the

892   challenges of an energy balance model for National Weather Service forecasts. J. Hydrol. 360

893   (1), 48–66. https://doi.org/10.1016/j.jhydrol.2008.07.013.

894   Franz, K.J., Butcher, P., Ajami, N.K., 2010. Addressing snow model uncertainty for hydrologic

895   prediction. Adv. Water Resour. 33 (8), 820–832.

896   https://doi.org/10.1016/j.advwatres.2010.05.004.

897   Frei, A., Tedesco, M., Lee, S., Foster, J., Hall, D.K., Kelly, R., Robinson, D.A., 2012. A review of

898   global satellite-derived snow products. Adv. Space Res. 50 (8), 1007–1029.

899   https://doi.org/10.1016/j.asr.2011.12.021.

900   Gan, Y., Liang, X.-Z., Duan, Q., Ye, A., Di, Z., Hong, Y., Li, J., 2018. A systematic assessment

901   and reduction of parametric uncertainties for a distributed hydrological model. J. Hydrol. 564,

902   697–711. https://doi.org/10.1016/j.jhydrol.2018.07.055.

903   Gan, Y., Liang, X.-Z., Duan, Q., Chen, F., Li, J., Zhang, Y., 2019. Assessment and reduction of

904   the physical parameterization uncertainty for Noah-MP land surface model. Water Resour.

905   Res. 55 (7), 5518–5538. https://doi.org/10.1029/2019WR024814.

906   Gan, Y., Zhang, Y., Kongoli, C., Grassotti, C., Liu, Y., Lee, Y., Seo, D.-J., 2021. Evaluation and

907   blending of ATMS and AMSR2 snow water equivalent retrievals over the conterminous

908   United States. Remote Sens. Environ. 254, 112280. https://doi.org/10.1016/j.rse.2020.112280.

909   Gandin, L.S., 1965. Objective Analysis of Meteorological Fields. Israel Program for Scientific

910   Translations, Jerusalem.

911   Gelb, A., 1974. Applied optimal estimation. MIT press, Cambridge, Massachusetts.

912   Gochis, D.J., Barlage, M., Dugger, A., FitzGerald, K., Karsten, L., McAllister, M., McCreight, J.,

913   Mills, J., RafieeiNasab, A., Read, L., Sampson, K., Yates, D., Yu, W., 2018. The WRF-Hydro

914   modeling system technical description, (Version 5.0). National Center for Atmospheric

915   Research, Boulder, Colorado. https://doi.org/10.5065/D6J38RBJ.

916 Gyawali, R., Watkins, D.W., 2013. Continuous hydrologic modeling of snow-affected watersheds

917   in the Great Lakes basin using HEC-HMS. J. Hydrol. Eng. 18 (1), 29–39.

918   https://doi.org/10.1061/(ASCE)HE.1943-5584.0000591.

919 Hedrick, A., Marshall, H.P., Winstral, A., Elder, K., Yueh, S., Cline, D., 2015. Independent

920   evaluation of the SNODAS snow depth product using regional-scale lidar-derived

921   measurements. The Cryosphere 9 (1), 13–23. https://doi.org/10.5194/tc-9-13-2015.

922 Hedrick, A.R., Marks, D., Havens, S., Robertson, M., Johnson, M., Sandusky, M., Marshall, H.,

923   Kormos, P.R., Bormann, K.J., Painter, T.H., 2018. Direct insertion of NASA Airborne Snow

924   Observatory-derived snow depth time series into the iSnobal energy balance snow model.

925   Water Resour. Res. 54 (10), 8045–8063. https://doi.org/10.1029/2018WR023190.

926 Hedstrom, N.R., Pomeroy, J.W., 1998. Measurements and modelling of snow interception in the

927   boreal forest. Hydrol. Process. 12 (10–11), 1611–1625. https://doi.org/10.1002/(SICI)1099-

928   1085(199808/09)12:10/11<1611::AID-HYP684>3.0.CO;2-4.

929 Helmert, J., Şensoy Şorman, A., Alvarado Montero, R., De Michele, C., De Rosnay, P., Dumont,

930   M., Finger, C.D., Lange, M., Picard, G., Potopová, V., Pullen, S., Vikhamar-Schuler, D.,

931   Arslan, N.A., 2018. Review of snow data assimilation methods for hydrological, land surface,

932   meteorological and climate models: Results from a COST HarmoSnow survey. Geosciences

933   8 (12), 489. https://doi.org/10.3390/geosciences8120489.

934   Henn, B., Newman, A.J., Livneh, B., Daly, C., Lundquist, J.D., 2018. An assessment of differences

935   in gridded precipitation datasets in complex terrain. J. Hydrol. 556, 1205–1219.

936   https://doi.org/10.1016/j.jhydrol.2017.03.008.

937   Hollingsworth, A., Lönnberg, P., 1986. The statistical structure of short-range forecast errors as

938   determined from radiosonde data. Part I: The wind field. Tellus A 38A (2), 111–136.

939   https://doi.org/10.1111/j.1600-0870.1986.tb00460.x.

940   Huang, C., Newman, A.J., Clark, M.P., Wood, A.W., Zheng, X., 2017. Evaluation of snow data

941   assimilation using the ensemble Kalman filter for seasonal streamflow prediction in the

942   western United States. Hydrol. Earth Syst. Sc. 21 (1), 635–650. https://doi.org/10.5194/hess-

943   21-635-2017.

944   Järvinen, H., 2001. Temporal evolution of innovation and residual statistics in the ECMWF

945   variational data assimilation systems. Tellus A: Dynamic Meteorology and Oceanography 53

946   (3), 333–347. https://doi.org/10.3402/tellusa.v53i3.12192.

947   Jordan, R.E., 1991. A one-dimensional temperature model for a snow cover: Technical

948   documentation for SNTHERM.89. Cold Region Research and Engineering Laboratory, U.S.

949   Army Corps of Engineers, Hanover, New Hampshire.

950   Kalman, R.E., 1960. A new approach to linear filtering and prediction problems. Journal of Basic

951   Engineering 82 (1), 35–45. https://doi.org/10.1115/1.3662552.

952   Kelly, R., 2009. The AMSR-E snow depth algorithm: Description and initial results. J. Remote

953   Sens. Soc. Japan 29 (1), 307–317. https://doi.org/10.11440/rssj.29.307.

954   Kumar, S.V., Peters-Lidard, C.D., Mocko, D., Reichle, R., Liu, Y., Arsenault, K.R., Xia, Y., Ek,

955   M., Riggs, G., Livneh, B., Cosh, M., 2014. Assimilation of remotely sensed soil moisture and

956   snow depth retrievals for drought estimation. J. Hydrometeorol. 15 (6), 2446–2469.

957   https://doi.org/10.1175/JHM-D-13-0132.1.

958   Kumar, S.V., Mocko, D., Vuyovich, C., Peters-Lidard, C., 2020. Impact of surface albedo

959   assimilation on snow estimation. Remote Sens. 12 (4), 645.

960   https://doi.org/10.3390/rs12040645.

961   Kwon, Y., Yang, Z.-L., Hoar, T.J., Toure, A.M., 2017. Improving the radiance assimilation

962   performance in estimating snow water storage across snow and land-cover types in North

963   America. J. Hydrometeorol. 18 (3), 651–668. https://doi.org/10.1175/JHM-D-16-0102.1.

964   Li, D., Durand, M., Margulis, S.A., 2017. Estimating snow water equivalent in a Sierra Nevada

965   watershed via spaceborne radiance data assimilation. Water Resour. Res. 53 (1), 647–671.

966   https://doi.org/10.1002/2016WR018878.

967   Lievens, H., Demuzere, M., Marshall, H., Reichle, R.H., Brucker, L., Brangers, I., de Rosnay, P.,

968   Dumont, M., Girotto, M., Immerzeel, W.W., Jonas, T., Kim, E.J., Koch, I., Marty, C.,

969   Saloranta, T., Schöber, J., De Lannoy, G.J.M., 2019. Snow depth variability in the Northern

970   Hemisphere mountains observed from space. Nat. Commun. 10 (1), 4629.

971   https://doi.org/10.1038/s41467-019-12566-y.

972   Liston, G.E., Elder, K., 2006. A meteorological distribution system for high-resolution terrestrial

973   modeling (MicroMet). J. Hydrometeorol. 7 (2), 217–234. https://doi.org/10.1175/JHM486.1.

974   Liston, G.E., Hiemstra, C.A., 2008. A simple data assimilation system for complex snow

975   distributions (SnowAssim). J. Hydrometeorol. 9 (5), 989–1004.

976   https://doi.org/10.1175/2008JHM871.1.

977   Liu, Y., Weerts, A.H., Clark, M., Hendricks Franssen, H.J., Kumar, S., Moradkhani, H., Seo, D.-

978   J., Schwanenberg, D., Smith, P., van Dijk, A.I.J.M., van Velzen, N., He, M., Lee, H., Noh,

979   S.J., Rakovec, O., Restrepo, P., 2012. Advancing data assimilation in operational hydrologic

980   forecasting: progresses, challenges, and emerging opportunities. Hydrol. Earth Syst. Sc. 16

981   (10), 3863–3887. https://doi.org/10.5194/hess-16-3863-2012.

982   Liu, Y., Peters-Lidard, C.D., Kumar, S., Foster, J.L., Shaw, M., Tian, Y., Fall, G.M., 2013.

983   Assimilating satellite-based snow depth and snow cover products for improving snow

984   predictions in Alaska. Adv. Water Resour. 54, 208–227.

985   https://doi.org/10.1016/j.advwatres.2013.02.005.

986   Liu, Y., Peters-Lidard, C.D., Kumar, S.V., Arsenault, K.R., Mocko, D.M., 2015. Blending

987   satellite-based snow depth products with in situ observations for streamflow predictions in the

988   Upper Colorado River Basin. Water Resour. Res. 51 (2), 1182–1202.

989   https://doi.org/10.1002/2014WR016606.

990   Lohmann, D., Mitchell, K.E., Houser, P.R., Wood, E.F., Schaake, J.C., Robock, A., Cosgrove,

991   B.A., Sheffield, J., Duan, Q., Luo, L., Higgins, R.W., Pinker, R.T., Tarpley, J.D., 2004.

992   Streamflow and water balance intercomparisons of four land surface models in the North

993   American Land Data Assimilation System project. J. Geophys. Res. 109, D07S91.

994   https://doi.org/10.1029/2003JD003517.

995   Magnusson, J., Gustafsson, D., Hüsler, F., Jonas, T., 2014. Assimilation of point SWE data into a

996   distributed snow cover model comparing two contrasting methods. Water Resour. Res. 50

997   (10), 7816–7835. https://doi.org/10.1002/2014WR015302.

998   Magnusson, J., Wever, N., Essery, R., Helbig, N., Winstral, A., Jonas, T., 2015. Evaluating snow

999   models with varying process representations for hydrological applications. Water Resour. Res.

1000   51 (4), 2707–2723. https://doi.org/10.1002/2014WR016498.

1001   Magnusson, J., Winstral, A., Stordal, A.S., Essery, R., Jonas, T., 2017. Improving physically based

1002   snow simulations by assimilating snow depths using the particle filter. Water Resour. Res. 53

1003   (2), 1125–1143. https://doi.org/10.1002/2016WR019092.

1004   Malik, M.J., van der Velde, R., Vekerdy, Z., Su, Z., 2012. Assimilation of satellite-observed snow

1005   albedo in a land surface model. J. Hydrometeorol. 13 (3), 1119–1130.

1006   https://doi.org/10.1175/JHM-D-11-0125.1.

1007   McKay, L., Bondelid, T., Dewald, T., Johnston, J., Moore, R., Rea, A., 2012. NHDPlus Version

1008   2: User Guide. U.S. Environmental Protection Agency.

1009   Molotch, N.P., Painter, T.H., Bales, R.C., Dozier, J., 2004. Incorporating remotely-sensed snow

1010   albedo into a spatially-distributed snowmelt model. Geophys. Res. Lett. 31 (3), L03501.

1011   https://doi.org/10.1029/2003GL019063.

National Centers for Environmental Prediction/National Weather Service/NOAA/U.S. Department of Commerce, 2000. NCEP FNL Operational Model Global Tropospheric Analyses, continuing from July 1999. Research Data Archive at the National Center for Atmospheric Research, Computational and Information Systems Laboratory, Boulder, CO. https://doi.org/10.5065/D6M043C6.

Niu, G.-Y., Yang, Z.-L., 2004. Effects of vegetation canopy processes on snow surface energy and mass balances. J. Geophys. Res. Atmos. 109, D23111. https://doi.org/10.1029/2004JD004884.

Niu, G.-Y., Yang, Z.-L., 2007. An observation-based formulation of snow cover fraction and its evaluation over large North American river basins. J. Geophys. Res. Atmos. 112, D21101. https://doi.org/10.1029/2007JD008674.

Niu, G.-Y., Yang, Z.-L., Mitchell, K.E., Chen, F., Ek, M.B., Barlage, M., Kumar, A., Manning, K., Niyogi, D., Rosero, E., 2011. The community Noah land surface model with multiparameterization options (Noah-MP): 1. Model description and evaluation with local-scale measurements. J. Geophys. Res. Atmos. 116, D12109. https://doi.org/10.1029/2010JD015139.

Painter, T.H., Berisford, D.F., Boardman, J.W., Bormann, K.J., Deems, J.S., Gehrke, F., Hedrick, A., Joyce, M., Laidlaw, R., Marks, D., Mattmann, C., McGurk, B., Ramirez, P., Richardson, M., Skiles, S.M., Seidel, F.C., Winstral, A., 2016. The Airborne Snow Observatory: Fusion of scanning lidar, imaging spectrometer, and physically-based modeling for mapping snow

water equivalent and snow albedo. Remote Sens. Environ. 184, 139–152. https://doi.org/10.1016/j.rse.2016.06.018.

Petersky, R., Harpold, A., 2018. Now you see it, now you don't: a case study of ephemeral snowpacks and soil moisture response in the Great Basin, USA. Hydrol. Earth Syst. Sc. 22 (9), 4891–4906. https://doi.org/10.5194/hess-22-4891-2018.

Pulliainen, J., Luojus, K., Derksen, C., Mudryk, L., Lemmetyinen, J., Salminen, M., Ikonen, J., Takala, M., Cohen, J., Smolander, T., Norberg, J., 2020. Patterns and trends of Northern Hemisphere snow mass from 1980 to 2018. Nature 581 (7808), 294–298. https://doi.org/10.1038/s41586-020-2258-0.

RafieeiNasab, A., Karsten, L., Dugger, A., FitzGerald, K., Cabell, R., Gochis, D., Yates, D., Sampson, K., McCreight, J., Read, L., Zhang, Y., McAllister, M., 2020. Overview of National Water Model Calibration General Strategy & Optimization. National Center for Atmospheric Research, Boulder, Colorado. Available online: https://ral.ucar.edu/sites/default/files/public/projects/wrf-hydro/training-materials/calibrationnov2020-arezoo.pdf.

Raleigh, M.S., Lundquist, J.D., Clark, M.P., 2015. Exploring the impact of forcing error characteristics on physically based snow simulations within a global sensitivity analysis framework. Hydrol. Earth Syst. Sc. 19 (7), 3153–3179. https://doi.org/10.5194/hess-19-3153-2015.

1050   Sampson, K., Gochis, D., 2020. WRF Hydro GIS Pre-Processing Tools, Version 5.1.1

1051   Documentation. National Center for Atmospheric Research, Boulder, Colorado.

1052   Sasaki, Y., 1958. An objective analysis based on the variational method. Journal of the

1053   Meteorological Society of Japan. Ser. II 36 (3), 77–88.

1054   https://doi.org/10.2151/jmsj1923.36.3_77.

1055   Smyth, E.J., Raleigh, M.S., Small, E.E., 2020. Improving SWE estimation with data assimilation:

1056   The influence of snow depth observation timing and uncertainty. Water Resour. Res. 56 (5),

1057   e2019WR026853. https://doi.org/10.1029/2019WR026853.

1058   Stewart, L.M., Dance, S.L., Nichols, N.K., 2013. Data assimilation with correlated observation

1059   errors: experiments with a 1-D shallow water model. Tellus A: Dynamic Meteorology and

1060   Oceanography 65 (1), 19546. https://doi.org/10.3402/tellusa.v65i0.19546.

1061   Stewart, L.M., Dance, S.L., Nichols, N.K., Eyre, J.R., Cameron, J., 2014. Estimating interchannel

1062   observation-error correlations for IASI radiance data in the Met Office system†. Q. J. Roy.

1063   Meteor. Soc. 140 (681), 1236–1244. https://doi.org/https://doi.org/10.1002/qj.2211.

1064   Sturm, M., Holmgren, J., Liston, G.E., 1995. A seasonal snow cover classification system for local

1065   to global applications. J. Climate 8 (5), 1261–1283. https://doi.org/10.1175/1520-

1066   0442(1995)008<1261:ASSCCS>2.0.CO;2.

1067   Sturm, M., Taras, B., Liston, G.E., Derksen, C., Jonas, T., Lea, J., 2010. Estimating snow water

1068   equivalent using snow depth data and climate classes. J. Hydrometeorol. 11 (6), 1380–1394.

1069   https://doi.org/10.1175/2010JHM1202.1.

1070   Suriano, Z.J., Henderson, G.R., Leathers, D.J., 2020. Discharge responses associated with rapid

1071   snow cover ablation events in the Susquehanna and Wabash River basins. Phys. Geogr. 41

1072   (1), 70–82. https://doi.org/10.1080/02723646.2019.1674558.

1073   Talagrand, O., Miyakoda, K., 1971. The assimilation of past data in dynamical analysis. II. Tellus

1074   23 (4–5), 318–327. https://doi.org/10.1111/j.2153-3490.1971.tb00578.x.

1075   Tangdamrongsub, N., Steele-Dunne, S.C., Gunter, B.C., Ditmar, P.G., Weerts, A.H., 2015. Data

1076   assimilation of GRACE terrestrial water storage estimates into a regional hydrological model

1077   of the Rhine River basin. Hydrol. Earth Syst. Sc. 19 (4), 2079–2100.

1078   https://doi.org/10.5194/hess-19-2079-2015.

1079   Terzago, S., Andreoli, V., Arduini, G., Balsamo, G., Campo, L., Cassardo, C., Cremonese, E.,

1080   Dolia, D., Gabellani, S., von Hardenberg, J., Morra Di Cella, U., Palazzi, E., Piazzi, G.,

1081   Pogliotti, P., Provenzale, A., 2020. Sensitivity of snow models to the accuracy of

1082   meteorological forcings in mountain environments. Hydrol. Earth Syst. Sc. 24 (8), 4061–4090.

1083   https://doi.org/10.5194/hess-24-4061-2020.

1084   Teweldebrhan, A.T., Burkhart, J.F., Schuler, T.V., Xu, C., 2019. Improving the informational

1085   value of MODIS fractional snow cover area using fuzzy logic based ensemble smoother data

1086   assimilation frameworks. Remote Sens. 11 (1), 28. https://doi.org/10.3390/rs11010028.

1087   Thirel, G., Salamon, P., Burek, P., Kalas, M., 2013. Assimilation of MODIS snow cover area data

1088   in a distributed hydrological model using the particle filter. Remote Sens. 5 (11), 5825–5850.

1089   https://doi.org/10.3390/rs5115825.

1090   Toure, A.M., Reichle, R.H., Forman, B.A., Getirana, A., De Lannoy, G.J.M., 2018. Assimilation

1091   of MODIS snow cover fraction observations into the NASA catchment land surface model.

1092   Remote Sens. 10 (2), 316. https://doi.org/10.3390/rs10020316.

1093   Waller, J.A., Dance, S.L., Nichols, N.K., 2016. Theoretical insight into diagnosing observation

1094   error correlations using observation-minus-background and observation-minus-analysis

1095   statistics. Q. J. Roy. Meteor. Soc. 142 (694), 418–431. https://doi.org/10.1002/qj.2661.

1096   Wang, T., Peng, S., Krinner, G., Ryder, J., Li, Y., Dantec-Nédélec, S., Ottlé, C., 2015. Impacts of

1097   satellite-based snow albedo assimilation on offline and coupled land surface model

1098   simulations. PLoS One 10 (9), e0137275. https://doi.org/10.1371/journal.pone.0137275.

1099   Wang, W., Bruyère, C., Duda, M., Dudhia, J., Gill, D., Kavulich, M., Keene, K., Chen, M., Lin,

1100   H., Michalakes, J., Rizvi, S., Zhang, X., Berner, J., Ha, S., Fossell, K., 2017. ARW version 3

1101   modeling system user's guide. National Center for Atmosphere Research, Boulder, CO.

1102   Weng, F., Zou, X., Wang, X., Yang, S., Goldberg, M.D., 2012. Introduction to Suomi national

1103   polar-orbiting partnership advanced technology microwave sounder for numerical weather

1104   prediction and tropical cyclone applications. J. Geophys. Res. Atmos. 117, D19112.

1105   https://doi.org/10.1029/2012JD018144.

1106   Wrzesien, M.L., Durand, M.T., Pavelsky, T.M., Howat, I.M., Margulis, S.A., Huning, L.S., 2017.

1107   Comparison of methods to estimate snow water equivalent at the mountain range scale: A

1108   case study of the California Sierra Nevada. J. Hydrometeorol. 18 (4), 1101–1119.

1109   https://doi.org/10.1175/JHM-D-16-0246.1.

1110 Xia, Y., Mitchell, K., Ek, M., Sheffield, J., Cosgrove, B., Wood, E., Luo, L., Alonge, C., Wei, H.,

1111 Meng, J., Livneh, B., Lettenmaier, D., Koren, V., Duan, Q., Mo, K., Fan, Y., Mocko, D.,

1112 2012a. Continental-scale water and energy flux analysis and validation for the North

1113 American Land Data Assimilation System project phase 2 (NLDAS-2): 1. Intercomparison

1114 and application of model products. J. Geophys. Res. Atmos. 117, D03109.

1115 https://doi.org/10.1029/2011JD016048.

1116 Xia, Y., Mitchell, K., Ek, M., Cosgrove, B., Sheffield, J., Luo, L., Alonge, C., Wei, H., Meng, J.,

1117 Livneh, B., Duan, Q., Lohmann, D., 2012b. Continental-scale water and energy flux analysis

1118 and validation for North American Land Data Assimilation System project phase 2 (NLDAS-

1119 2): 2. Validation of model-simulated streamflow. J. Geophys. Res. 117, D03110.

1120 https://doi.org/10.1029/2011JD016051.

1121 Yan, H., Moradkhani, H., 2016. Combined assimilation of streamflow and satellite soil moisture

1122 with the particle filter and geostatistical modeling. Adv. Water Resour. 94, 364–378.

1123 https://doi.org/10.1016/j.advwatres.2016.06.002.

1124 Yang, Z.-L., Dickinson, R.E., Robock, A., Vinnikov, K.Y., 1997. Validation of the snow submodel

1125 of the Biosphere–Atmosphere Transfer Scheme with Russian snow cover and meteorological

1126 observational data. J. Climate 10 (2), 353–373. https://doi.org/10.1175/1520-

1127 0442(1997)010<0353:VOTSSO>2.0.CO;2.

1128 Yang, Z.-L., Niu, G.-Y., 2003. The versatile integrator of surface and atmosphere processes. Part

1129 1. Model description. Global Planet. Change 38 (1–2), 175–189.

1130 https://doi.org/10.1016/S0921-8181(03)00028-6.

1131 Yang, Z.-L., Cai, X., Zhang, G., Tavakoly, A.A., Jin, Q., Meyer, L.H., Guan, X., 2011. The

1132 community Noah land surface model with multi-parameterization options (Noah-MP). The

1133 University of Texas at Austin, Austin, TX.

1134 Zaitchik, B.F., Rodell, M., 2009. Forward-looking assimilation of MODIS-derived snow-covered

1135 area into a land surface model. J. Hydrometeorol. 10 (1), 130–148.

1136 https://doi.org/10.1175/2008JHM1042.1.

1137 Zhang, G., Chen, F., Gan, Y., 2016. Assessing uncertainties in the Noah-MP ensemble simulations

1138 of a cropland site during the Tibet Joint International Cooperation program (JICA) field

1139 campaign. J. Geophys. Res. Atmos. 121 (16), 9576–9596.

1140 https://doi.org/10.1002/2016JD024928.

1141 Zhang, Y., Hoar, T.J., Yang, Z.-L., Anderson, J.L., Toure, A.M., Rodell, M., 2014. Assimilation

1142 of MODIS snow cover through the Data Assimilation Research Testbed and the Community

1143 Land Model version 4. J. Geophys. Res. Atmos. 119 (12), 7091–7103.

1144 https://doi.org/10.1002/2013JD021329.

1145 Zhang, Y., Grimm, J., Cabell, R., Gochis, D., Petzke, B., Fall, G., Kitzmiller, D., 2020. WRF-

1146 Hydro Forcing Engine Overview. National Center for Atmospheric Research, Boulder,

1147   Colorado. Available online: https://ral.ucar.edu/sites/default/files/public/projects/wrf-

1148   hydro/training-materials/8forcing-overview-forcing-cuahsi-nov2020.pdf.

1149